

# Bubble migration in a turbulent boundary layer

S. Tran-Cong, J.L. Marié\*, R.J. Perkins

*Laboratoire de Mécanique des Fluides et d'Acoustique, Université de Lyon, France  
CNRS – École centrale de Lyon, Université Claude Bernard Lyon I, Insa de Lyon ECL, 36 Avenue Guy de Collongue,  
69134 Ecully Cedex, France*

Received 12 January 2007; received in revised form 3 December 2007

## Abstract

The wall void peaking distribution observed in an upward turbulent bubbly boundary layer along a flat plate is generated by bubbles that move towards the plate, come into contact with the wall and then slide along it. This transverse ‘migration’ has been studied using flow visualization, high speed video and particle tracking techniques to measure the trajectories of mono-disperse air bubbles at very low void fractions. Investigations have been performed at four Reynolds numbers in the range  $280 < Re_\theta < 3000$ , covering both the laminar and turbulent regimes, with mono-disperse bubbles of mean equivalent diameter between 2 mm and 6 mm. Lagrangian statistics calculated from hundreds of trajectories show that the migration only occurs in the turbulent regime and for bubble diameters below some critical value:  $3.5 \text{ mm} < d_{\text{eqcrit}} < 4 \text{ mm}$ . Above this size ( $We > 3$ ), the interface deformation is such that bubbles do not remain at the wall, even when they are released at the surface. Also, bubble migration is shown to be non-systematic, to have a non-deterministic character in the sense that trajectories differ significantly, to increase with Reynolds number and to take place on a short time scale. A series of experiments with isolated bubbles demonstrates that these results are not influenced by bubble–bubble interactions and confirm that two-way coupling in the flow is limited. Flow visualizations show that the migration originates with the capture of bubbles inside the large turbulent structures of the boundary layer (‘bulges’). The bubbles begin to move towards the wall as they cross these structures, and the point at which they reach the wall is strongly correlated with the position of the deep ‘valleys’ which separate the turbulent ‘bulges’. The analysis of the mean Lagrangian trajectories of migrating bubbles confirms these observations. Firstly, the average time of migration calculated from these trajectories coincides with the mean transit time of the bubbles across the structures. Secondly, once the trajectories have been scaled by this transit time and the boundary layer thickness  $\delta$ , they all have the same form in the region  $y/\delta < 0.4$ , independent of the Reynolds number.

© 2008 Elsevier Ltd. All rights reserved.

**Keywords:** Void fraction distribution; Bubbly turbulent boundary layer; Bubble migration; Coherent structures

## 1. Introduction

It is now well established that the void fraction distribution in wall bounded turbulent bubbly flows is generally non-uniform, even for the simplest geometries. This spatial non uniformity results mainly from the preferential transport and accumulation of bubbles in certain regions of the flow, and this can modify the local structure of the boundary layer, mass and momentum transfer at the wall, and the production of turbulence. Understanding the mechanisms

that drive bubble motion in such turbulent flows is therefore crucial for a number of engineering processes, including mixing, drag and heat transfer. It constitutes an essential step in the modelling of multiphase dispersed systems. The objective of the present work is to investigate the mechanisms underlying bubble migration for the specific case of an up-flowing turbulent boundary layer along a flat plate.

Most of the experiments on the bubble distribution in wall bounded turbulent flows have been performed in internal geometries – pipe or channel flows – with significantly poly-dispersed ellipsoidal bubbles, in non-dilute regimes (void fraction  $\varepsilon > 1\%$ ) and steady conditions, using Eulerian measurement techniques (resistance, optical or hot film

\* Corresponding author. Tel.: +33 4 72 18 61 66; fax: +33 4 78 64 71 45.  
E-mail address: [jean-louis.marie@ec-lyon.fr](mailto:jean-louis.marie@ec-lyon.fr) (J.L. Marié).

probes). Serizawa and Kataoka (1988) and Liu (1993, 1997) provide comprehensive surveys of these studies. They show that in upward flows a high percentage of bubbles can be found at the wall, in the core or in both regions, generating respectively wall-peaking, coring or intermediate (saddle shape) void distributions (Serizawa et al., 1975; Herringe and Davis, 1976; Nakoryakov et al., 1981; Wang et al., 1987; Liu, 1993; Grossetete, 1995). The type of distribution which develops depends strongly on the bubble size, which is determined by the inlet conditions and by the subsequent coalescence and break-up of the bubbles. The data indicate that small bubbles concentrate near the walls, whereas the larger ones congregate in the core. This is not true for downward flows, where bubbles accumulate in the core whatever their size (Ganchev and Peresadko, 1985; Wang et al., 1987; Kashinsky and Randin, 1999). The physical mechanisms that produce these void fraction distributions have been studied experimentally by Sekoguchi et al. (1974), Sato et al. (1976), and Sekoguchi et al. (1979), using flow visualization and photographic techniques to record bubble motion. Those studies were carried out in a square channel with nearly mono-disperse bubbles released from a single nozzle at low concentrations. They showed that in upward flow smaller bubbles ( $d_{eq} < 5$  mm) migrate towards the wall and slide along it (motion at the origin of the wall-peaking), whereas the larger bubbles ( $d_{eq} > 5$  mm) move into the core of the flow with spiralling or rocking trajectories. Bubble migration, and in particular the subsequent sliding along the wall, has never been observed in downward flow, whatever the bubble size. Zun (1980, 1988, 1990) performed similar experiments in upward flow, with an improved system of bubble injection, to provide better control of bubble sizes. Bubble trajectories and bubble migration were measured using a combination of bubble counting, void fraction measurements and photographic imaging of the flow. For a flow Reynolds number  $Re = 10,000$  (Zun, 1988) he identified five distinct regimes of bubble motion, as a function of equivalent bubble diameter  $d_{eq}$ :

- $d_{eq} < 0.6$  mm: bubbles accumulate in the centre of the pipe ('coring'),
- $0.6$  mm  $< d_{eq} < 0.8$  mm: transitional distribution, from coring to wall peaking,
- $0.8$  mm  $< d_{eq} < 3.6$  mm: bubbles accumulate at the wall ('wall peaking'),
- $3.6$  mm  $< d_{eq} < 5.1$  mm: transitional distribution, from wall peaking to coring,
- $d_{eq} > 5.1$  mm: bubbles accumulate in the centre of the pipe.

The important point to note here is that the diameter range where the migration is significant corresponds to bubbles which intrinsically oscillate in quiescent water.

Although a wide variety of flow conditions have been documented in these experiments, it is difficult to conclude as to the exact causes of the different distributions that have been observed. In particular, the question of wall

migration has been at the origin of much controversy, and several different explanations have been proposed, including bubble dynamics in a shear flow (bubble lift forces, interface deformation, and wake), the turbulence in the flow (turbulence gradients, weak pressure gradients, and eddy dynamics), the vicinity of the wall (wall forces), or a coupling between these effects. Of these different explanations the lift force due to the interaction between bubble drift and vorticity in the flow is the most frequently cited, since, in principle it can explain the difference in bubble migration as the flow switches from upflow to downflow. For upflow the relative velocity of the bubble and the vorticity in the flow combine to push bubbles towards the wall. When the flow direction changes, the vorticity changes sign but the relative velocity of the bubble does not, so the lift force changes sign and bubbles are pushed towards the centre of the pipe. But although the predictions of the theory are in qualitative agreement with observations, it is much more difficult to obtain quantitative agreement. Away from the wall the vorticity in the flow is relatively weak, and neither the force derived by Saffman (1965) nor that derived by Auton et al. (1988) is sufficient to explain the initial stages of bubble migration that have been observed experimentally. Nor do these theories explain the observed dependence on bubble size. The mean shear in the flow can also act directly to deform the bubble and its wake; this can modify the circulation round the bubble and lead to a reversal of the lift, as is the case in laminar shear flow (Kariyasaki, 1987). This could explain why large bubbles migrate to the core of the flow. The turbulence in the liquid phase acts on both the bubble and the bubble wake and this modifies the instantaneous forces acting on the bubble; the transverse gradient in turbulent intensities can also generate a lateral lift ('turbophoresis') but would not change sign with a change in flow direction. Studies in zero gravity conditions (Colin et al., 1993) where the bubble relative velocity – and hence the inertial lift force – is zero, suggest that liquid turbulence acts to disperse the bubbles laterally throughout the pipe. Proximity to the wall could also modify the lateral movement of the bubbles; it generates a potential flow interaction with the bubble approaching the surface which according to bubble image theory, results in an attractive wall force (Milne-Thomson, 1968). However, very close to the wall other complex boundary phenomena such as the interaction of the bubble wake with the surface, collision with the wall, capillary waves and liquid film effects may dominate and generate repulsive forces.

To perform a more detailed investigation of bubble motion in wall-bounded turbulence, Moursali et al. (1995) and Marié et al. (1997) studied an upward turbulent bubbly boundary layer along a vertical flat plate. This configuration has several advantages: there is no turbulent far-field, it is possible to measure very close to the surface, and bubble injection can be controlled precisely. These studies measured void fraction distribution, wall transfer and mean liquid velocity and turbulence profiles. They showed that when

mono-dispersed ellipsoidal bubbles of 3–3.5 mm equivalent diameter are introduced in nearly dilute conditions ( $\varepsilon < 1.5\%$ ) upstream of the leading edge, there is a sharp peak in void fraction at the wall, at a distance somewhat greater than the bubble radius ( $\sim 0.65 d_{eq}$ ). At higher void fraction ( $\varepsilon > 3\%$ ), when the bubble size distribution broadens from 3 mm to 8 mm (average value 6 mm) with increasing gas-flow rate, the distribution gradually changes from wall-peaking to void-coring, as in pipe flow. High-speed video films of bubble motion close to the surface showed that the wall-peaking arises from the migration of the small bubbles towards the wall and their subsequent trapping at the surface. These migrations are non-systematic and occur on a short time scale, suggesting that the turbulence plays an important role in the motion towards the plate. This paper presents results of subsequent experiments performed to provide a more extensive Lagrangian description of the bubble motion and test the assumption concerning the turbulence. The originality of the study lies in the statistical analysis of the Lagrangian trajectories and in the simultaneous visualizations of bubble trajectories and the large scale structures in the boundary layer. Experiments were performed with mono-dispersed bubbles of increasing diameter from 2 mm to 6 mm, both in laminar and turbulent regime.

Recently, Felton and Loth (2001, 2002) also reported the results of a study of bubble motion in the boundary layer on a vertical flat plate. The phenomena they investigated are quite similar to those in this work, but concern spherical bubbles, for which interface deformation is weak and available data are scarce. The measurements were made in the dilute void fraction regime, using bubbles with diameters of 0.37–1.2 mm which were released from single needles, at various transverse wall-positions for free-stream Reynolds numbers between 13,000 and 20,000. Several different types of bubble motion were identified, depending on the Stokes number and the location of bubble injection. In general bubbles with high Stokes number (corresponding to larger bubbles or weaker turbulence) tended to collect at the wall, whilst bubbles with low Stokes number diffused throughout the boundary layer. The migration of individual bubbles towards the wall was then studied by a combination of PTV and PIV techniques. Typical sequences of events were identified from bubble trajectories, together with time-evolving liquid velocity fields. These tend to show that once bubbles have left the injector they disperse laterally in the turbulent boundary layer, until a sufficiently strong vortex inside the inner layer ( $y < 0.5\delta$ ) yields a lift force which is strong enough to cause them to migrate towards the wall. The mean lift forces computed from these data are consistent in magnitude and direction with the shear-induced lift forces reported in previous laminar experiments, to within the relative experimental uncertainty, which was estimated as 50%. This supports the idea that the main cause of wall-peaking in the inner layer is the lift generated by the eddies surrounding the bubbles. As a rule, the mean lift coefficients found in this study are closer to the values given by laminar theory or experiments, than those predicted by inviscid theory.

## 2. Experimental procedures

### 2.1. Boundary layer flow facility

The flow facility consists of a closed loop water tunnel which has been described in detail in Lance and Bataille (1991) and in Moursali et al. (1995). The loop consists essentially of a 50 m<sup>3</sup> water tank and a 2.5 m long vertical square channel with a cross-section measuring 400 mm  $\times$  400 mm. It was operated in the upward direction at atmospheric pressure and ambient temperature, at liquid velocities which did not exceed 1.5 m s<sup>-1</sup>. The water was filtered and decalcified, but given the overall volume of the facility, no other treatment was employed, so it is likely that the water contained residual impurities and that the bubble surfaces were contaminated. A smooth flat plate, 2 m long ( $x$ -direction), 0.4 m wide ( $z$ -direction) and 15 mm thick ( $y$ -direction) was placed at the centre of the test section, as indicated in Fig. 1a. The leading edge, which was ogive-shaped, was located 0.5 m downstream from the entrance to the test section. The transition from laminar to turbulent boundary layer was triggered by a rough abrasive ribbon, 40 mm wide and 1 mm high, glued to the surface immediately downstream of the leading edge. This abrasive ribbon was removed for the runs in the laminar regime. The flat plate was made of plexiglass to provide optical access. The large scale structures in the boundary layer were visualised using a fluorescent dye (Rhodamine B) which was injected into the boundary layer through a rectangular slot in the plate, 0.5 m downstream from the leading edge. This slot measured 0.4 mm wide in the  $x$  direction and 10 mm long in the  $z$  direction. Dye could be injected tangentially to the surface, in almost isokinetic conditions, to minimise disturbances to the viscous sub-layer. All the measurements reported hereafter were performed in an area located at  $X = 1$  m downstream from the leading edge.

### 2.2. Bubble injection systems

In the previous studies (Moursali et al., 1995; Marié et al., 1997), bubbles were injected uniformly, far upstream of the plate, over the entire cross-section of the channel.

Here, to investigate the bubble motion over a large range of bubble sizes, in nearly mono-disperse and dilute conditions, bubbles were released from a single injector. Two modes of injection were implemented so that bubbles could be released either in a continuous stream or individually. In the first case (Fig. 2a and b), the air delivered by a compressor was injected at constant flow rate through hypodermic needles with internal diameters,  $\phi_{int}$ , between 0.42 and 1.3 mm. Each needle produced a line of bubbles with an almost constant mean equivalent diameter  $d_{eq}$  and a regular injection frequency  $f_{inj}$ . With this method it was possible to produce bubbles with equivalent diameters of 2, 3, 3.5, 4, 5 and 6 mm. To improve the size control for the largest diameters ( $d_{eq} \geq 3$  mm,  $\phi_{int} \geq 0.8$  mm), it was necessary to add a small flat plate, 0.5 mm thick, 35 mm

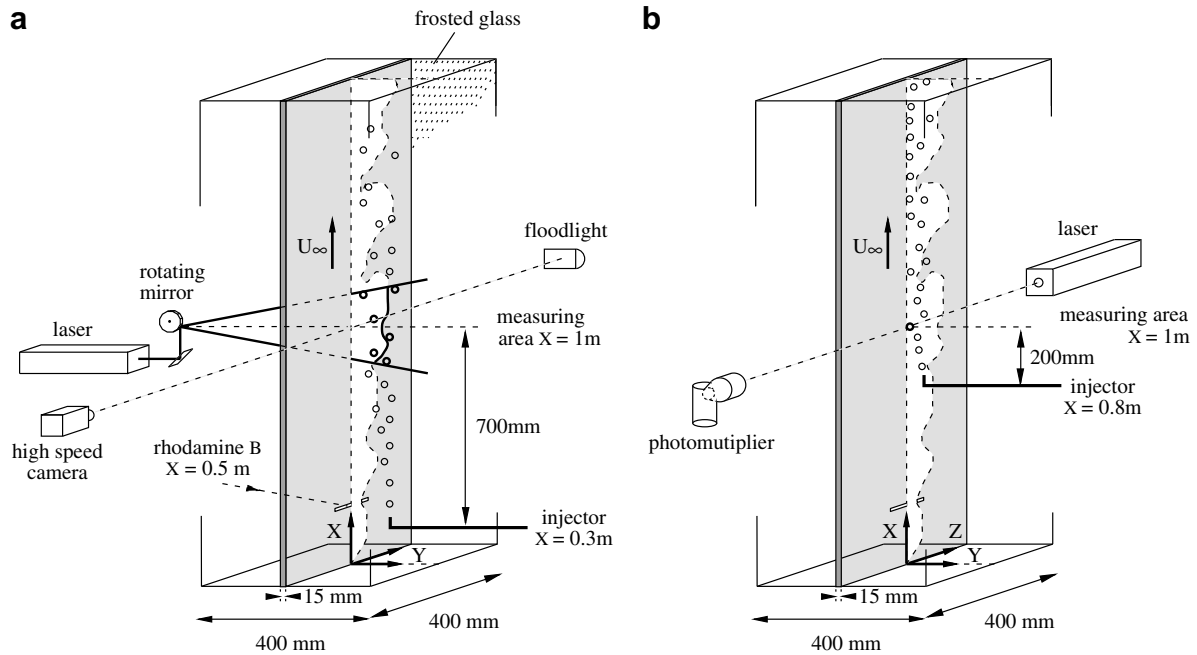


Fig. 1. Sketch of the plate and experimental techniques. (a) Visualization by shadowgraphy or fluorescent laser-sheet; (b) method for measuring the bubble trapping at the wall.

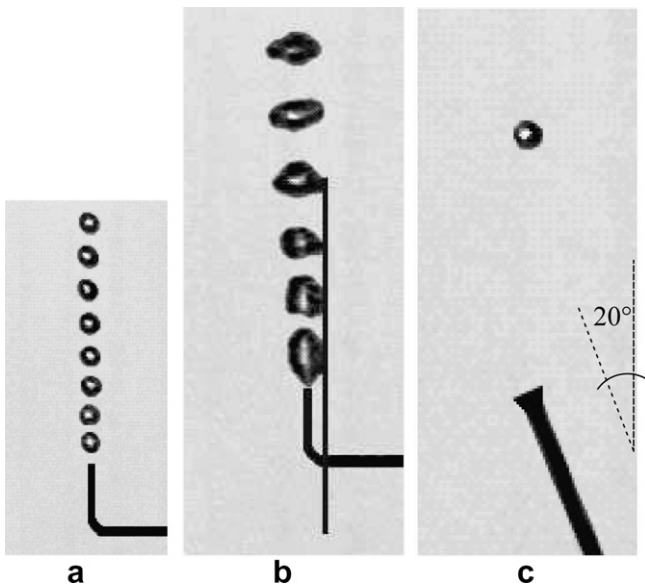


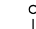
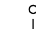

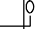

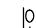
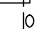
Fig. 2. The different bubble injectors. Injection at constant frequency: (a)  $d_{eq} = 2$  mm, (b)  $d_{eq} = 5$  mm; single injection: (c)  $d_{eq} = 3$  mm.  $U_{\infty} = 1$  m s<sup>-1</sup>.

long and 15 mm wide, near the needle exit tip (see Fig. 2b). The presence of this plate prevented the breakup of the bubbles at high liquid velocities and stabilized the bubble release frequency. The injection frequency was adjusted by varying the air flow rate, so as to obtain the required bubble diameter for a given free stream velocity. The injection parameters at  $U_{\infty} = 1.0$  m s<sup>-1</sup> are listed in Table 1. In the second mode, single bubbles were generated periodically, using by a rotating air–water distributor, which is

described in detail in Tran-Cong (1999). With this system, the injection process consisted of three steps: (i) a small volume of air was drawn into a closed cavity; (ii) water was introduced into the cavity to expel the air into a 3 mm flexible capillary, and (iii) the liquid and the air were injected together into the flow through a stainless tube (Fig. 2c). The external diameter of this tube was equal to 1.6 mm, and bubbles released from the end of the tube could have been trapped in its wake, so to avoid this, the tube was inclined at an angle of about 20° with respect to the vertical axis. In addition the tip of the tube was slightly widened to minimize the risk of bubble break up at the exit and the water flow rate inside was adjusted to release the bubble at a velocity close to the free stream velocity. The size of the bubble was determined by the choice of the volume of the cavity and the air pressure inside. The frequency of the bubble generation cycle was sufficiently low (<0.1 Hz) to prevent any hydrodynamic interaction with the preceding bubble. However, this system proved to be rather delicate and time-consuming to manipulate, so its use was restricted to one bubble diameter  $d_{eq} = 3$  mm and only a hundred realizations; this was still statistically sufficient to check whether the absence of bubble–bubble interaction has a significant effect on the migration.

In all flow visualizations, the single nozzle was located 0.7 m upstream of the measuring section (Fig. 1a) at a fixed distance from the wall  $Y_{inj}$ , of the order of 0.6–0.7 $\delta$ . This location was chosen to allow the bubbles to disperse in the free stream before entering the field of measurement; to ensure that bubbles would penetrate the outer edge of the boundary layer immediately upstream of the working area, whatever the flow conditions, and to give a mean void

Table 1  
Injection characteristics at  $U_\infty = 1 \text{ ms}^{-1}$ , for the case where bubbles are released continuously from a needle

Equivalent bubble diameter		Injector		Injection				Section $X = 1 \text{ m}$
$d_{\text{eq}}$ (mm)	$d_{\text{eq}}/\delta$	Nozzle geometry	Internal diameter	Position			Mean frequency	Bubble lateral dispersion
			$\phi_{\text{int}}$ (mm)	$X_{\text{inj}}$ (m)	$Y_{\text{inj}}$ (m)	$Y_{\text{inj}}/\delta$	$F_{\text{inj}}$ ( $\text{s}^{-1}$ )	$\Delta y$ (mm)
2	0.09		0.42	0.3	0.015	0.68	480	0.058
3	0.14		0.62	0.3	0.015	0.68	335	0.061
3.5	0.16		0.80	0.3	0.015	0.68	360	0.060
4	0.18		0.80	0.3	0.014	0.64	240	0.046
5	0.23		0.80	0.3	0.013	0.59	210	0.044
6	0.27		1.30	0.3	0.013	0.59	165	0.040

fraction in this area lower than 0.5% with the continuous injection mode, which means that bubble–bubble interactions and turbulence modifications were limited. However, to measure the bubble trapping at the wall as a function of the transverse bubble injection location in the boundary layer, the nozzle was positioned 0.2 m upstream of the measuring section (Fig. 1b). This reduced the lateral dispersion of the bubbles in the measuring section, so that there was less variation in the wall release distance, but it had the disadvantage that bubble–bubble interactions in the test area were more significant.

Bubble sizes for each test condition were measured from high speed video films taken with a small field of view to give sufficient spatial resolution, as described in the next section.

### 2.3. Instrumentation

As in the previous studies, the characteristics of the single-phase boundary layer were measured by LDV, using a 2.5 W Spectra Physics Argon laser (Stabilite 1016) and a TSI IFA550 fast auto-correlation processor.

Bubble motion and deformation were measured using a shadowgraph technique. The bubbles were filmed using a Kodak Ektapro EM 1012 high speed video camera (CCD  $192 \times 239$  pixels, 256 grey levels, up to 1000 frames/s), equipped with a 35–80 mm Tamron zoom objective. The optical configuration is shown in Fig. 1a. The camera and the lights were located on either side of the channel, facing each other and aligned with the  $z$ -direction. The flow was illuminated using two 500 W Halogen sources, behind frosted glass screens to diffuse the light; this minimises the optical distortion which might introduce errors into the measurements of the bubble contour (Lunde and Perkins, 1995). To obtain a good description of bubble outlines and trajectories, images were acquired at a rate of 500 frames/s, with a 1/1000 s exposure time, in half size format ( $96 \times 239$  pixels). This format was chosen because it covered the zone of interest in the flow ( $50 \text{ mm} \times 200 \text{ mm}$ ) and enabled us to maximise the duration of the recorded sequences; in this configuration we could record continuously for up to 1.6 s. The image resolution was not high

enough to permit the simultaneous measurement of bubble shape and bubble trajectory, so these were measured separately, using two different optical configurations. Bubble geometry was measured using a lens with a focal length of 60 mm and an aperture of  $f4$ – $5.6$ , giving a field of view of the order of  $75 \text{ mm} \times 30 \text{ mm}$  and a resolution of 0.31 mm/pixel. Bubble trajectories were measured using a lens with a focal length of 35 mm and an aperture of  $f4$ – $5.6$ , giving a field of view of the order of  $150 \text{ mm} \times 60 \text{ mm}$ . The image plane was calibrated by filming a grid placed in the object plane of the camera before each run. The calibration algorithm takes account of both camera position and inclination, and any distortion introduced by the optical properties of the camera lens and the different media between the camera and the object plane. After each run, the images stored in the camera buffer were transferred to videotape by means of an S-VHS VCR (Panasonic AG-7330). The images were then digitized on a PC equipped with a Data Translation DT 2861 image processing card ( $512 \times 512$  pixels, 256 grey levels) and a frame synchronizer type TBC. Once digitized, the images were treated using PTV software previously developed and tested by Perkins (Perkins and Hunt, 1989; Lunde and Perkins, 1995). This consisted essentially of two steps: (i) identification of the bubbles and determination of their contour, centre-coordinates, area and shape factor, (ii) tracking of the identified bubbles on consecutive frames and reconstruction of their trajectories. Detailed descriptions of the different procedures and algorithms used in this treatment are provided in Tran-Cong (1999).

As a check on the processing, the bubble size was estimated directly from the digital images before transfer to videotape. The optical configuration, with a single camera, only provided an image of the bubble projected onto the  $x$ – $y$  plane, so it was not possible to make a direct measurement of bubble volume. But the bubbles used in these experiments all fall in the oblate spheroid shape regime (Clift et al., 1978) so the bubble volume can be estimated from the measured length of the principal axis of the projected area, assuming that the bubble is indeed an oblate spheroid. The mean equivalent diameter  $d_{\text{eq}}$  can then be obtained from the bubble volume. To minimize the errors

introduced by this approach, measurements were restricted to bubbles in the free stream with their major axis perpendicular to the vertical (streamwise) direction. These bubbles have velocities that are approximately parallel to the main flow direction and outlines that are very close to elliptical. This method has been used by other researchers and its validity was recently discussed in Ellingsen and Risso (2001). The accuracy of the mean equivalent diameter measurements is difficult to quantify precisely. We can estimate that each contour point is detected by the CCD sensor with an error of  $\pm 1/2$  pixel, i.e.  $\pm 0.15$  mm. An error calculation on this basis yields an uncertainty of at most 10% in the estimate of the equivalent diameter of the smallest bubbles used in these experiments ( $d_{eq} = 2$  mm) and less than 7% for larger bubbles. But this calculation does not take into account the random way in which the errors in the different contour points are distributed, which means that in reality the accuracy should be significantly better than these estimates suggest. This is consistent with the observation that the standard deviation of these measurements remains small: less than 3% for small bubbles of diameter inferior to 3.5 mm and no more than 5% for larger bubbles. The uncertainty in the location of the bubble centre was estimated to be  $\pm 0.3$  mm, which represents about  $\pm 1.5\%$  of the boundary layer thickness. However, by smoothing the raw trajectories slightly, this was reduced to  $\pm 0.15$  mm. The bubble velocity was calculated from the smoothed trajectories by a finite difference approximation, with an uncertainty estimated at 6% for experiments with a free stream velocity of  $1 \text{ m s}^{-1}$ .

To investigate the possible effect of turbulent structures in the boundary layer on the migration of bubbles towards the walls, we performed some experiments with simultaneous visualization of the bubble trajectories and the unsteady structures in the boundary layer. These were visualised by injecting a fluorescent dye – Rhodamine B – into the boundary layer and illuminating the flow perpendicularly to the plate by a laser sheet (see Fig. 1a). It has been suggested that Rhodamine B acts as surfactant, making a bubble interface smoother, and reducing its oscillations. This could in turn have an effect on bubble migration. We did not attempt to quantify this effect for two reasons. Firstly as explained in Section 2.1, the water used in these experiments had not been purified, so it is likely that it

already contained significant quantities of surfactants, even before the addition of the Rhodamine B. Indeed, numerous studies have demonstrated significant differences between bubble rise velocities measured in ordinary tap water and those measured in highly purified water (Clift et al., 1978). Secondly, the migration rates measured after the addition of the Rhodamine B did not differ significantly from those previously without Rhodamine B, so we do not believe that any possible surfactant effect from the Rhodamine B was sufficient to modify the migration behaviour of the bubbles. As described in Section 2.1, the dye was released from a slot through the plate, tangentially to the surface, in almost isokinetic conditions. The laser sheet was generated with a rotating polygonal mirror located on the opposite side of the plate, so that the light sheet first passed through plate, before illuminating the flow in the boundary layer. This ensured that the shadows created by bubbles in the light sheet did not mask the flow in the region between the bubbles and the wall. The thickness of the laser sheet was adjusted by lenses to a value of  $500 \mu\text{m}$ , which was a compromise between the need for a thin sheet to provide good definition of the outlines of the turbulent structures in the boundary layer, and the need for a thick sheet to enable the tracking of the 3D motion of bubbles in the light plane. The Kodak Ektapro camera was not sufficiently sensitive at low light intensities, so the first visualizations were performed with a standard Sony V200E colour camera (CCD  $720 \times 640$  pixels, 50 frames/s, exposure time of  $1/500$  s). Given this low framing rate, the visualizations had to be performed at a rather low free stream velocity of  $0.5 \text{ m s}^{-1}$ , which was the upper limit for following the bubbles and the structures. These experiments were later completed by a second series of visualization at  $1 \text{ m s}^{-1}$ , with a more sensitive high speed video camera type Kodak Motion Corder SR-1000 (CCD  $512 \times 480$  pixels, 256 grey levels, 1000 frames/s, exposure time of  $1/1000$  s). In both cases, the camera was synchronized with the rotating mirror so that each frame corresponded to a single sweep of the laser beam. The flow conditions covered in the different studies are summarized in Table 2.

Finally the capture of the bubbles by the wall was also quantified by a classical attenuation technique using a laser beam. The beam was directed parallel to the plate ( $z$ -direction) at the point  $X = 1 \text{ m}$  and at a distance from the wall

Table 2  
Summary of the experimental runs:  $\times$  flow condition explored;  $\otimes$  computation of a mean migration trajectory; SB = single-bubble injector

$U_\infty$ ( $\text{m s}^{-1}$ )	$d_{eq}$ (mm)		SB				Type of camera
<i>Bubble trajectories</i>							
0.3	$\times$	–	–	$\times$	$\times$	$\times$	Kodak Ektapro EM 1012, $192 \times 239$ pix. 1000 frs $^{-1}$
0.5	$\otimes$	–	–	$\otimes$	$\times$	$\times$	
1.0	$\otimes$	$\otimes$	$\otimes$	$\otimes$	$\times$	$\times$	
1.5	$\otimes$	–	–	$\otimes$	$\times$	$\times$	
<i>Structure visualizations</i>							
0.5	–	$\times$	–	–	–	–	Sony V200E 50 frs $^{-1}$
1.0	–	$\times$	–	–	–	–	Kodak Motion Corder SR1000, $480 \times 512$ pix. 1000 frs $^{-1}$

( $\sim d_{\text{eq}}/2$ ) so that it would be intercepted by bubbles in contact with the surface (Fig. 1b). Bubbles crossing the beam attenuated the intensity of the transmitted light, and this was detected by a photomultiplier facing the laser source and aligned with its optical axis. The wall bubble frequency  $f_{\text{Bwall}}$  measured in this way was then normalized by the total number of bubbles  $f_{\text{inj}}$  injected into the flow during the same period, to obtain the wall-contact rate, as a func-

tion of bubble size and injection distance from the wall  $Y_{\text{inj}}$ . The bubble injection frequency  $f_{\text{inj}}$  was determined at the beginning of each run with a Photonetics optical probe positioned close to the nozzle exit, such that it did not affect the motion of the bubbles as they were released.

### 3. Results and discussion

#### 3.1. Reference flow characteristics

LDA measurements made in the absence of bubbles showed that the boundary layer had a standard structure in both laminar and turbulent regimes. The mean longitudinal velocity profiles were found self-similar and follow the expected laws, when plotted in the usual non dimensional forms. An example of dimensionless liquid velocity profiles at  $X = 1$  m is given in Fig. 3. Based on a statistical analysis of the LDV signal, we estimate that the relative uncertainty in the measured average velocities is of the order of 5%. The wall shear stress was measured using the techniques described in Moursali et al. (1995), for which the relative uncertainty was estimated as less than 10%. We can see that the profile at  $0.3 \text{ m s}^{-1}$  indeed follows the Blasius solution of laminar boundary layers, while those above  $0.5 \text{ m s}^{-1}$  exhibit the three classical zones: linear, logarithmic and wake laws (Schlichting, 1968). It should be noted that the logarithmic region at  $0.50 \text{ m s}^{-1}$  extends only up to  $Y^+ = 100$ , which is characteristic of a low Reynolds number post transitional boundary layer. In the deficit form, the same profiles fit the universal logarithmic law with a value of 2.35 for the constant, which is typical for boundary layers on flat plates, and we therefore conclude that there was no significant pressure gradient along the  $X$ -axis (Tennekes and Lumley, 1972). The longitudinal turbulence intensities profiles were also measured. The turbulence levels within the buffer layer were of the same order as the values generally reported in previous studies with the same Reynolds numbers, and lower than 1% in the free stream. The characteristics of the boundary layer at  $X = 1$  m, – its thickness,  $\delta$ , momentum thickness,  $\theta$ , friction velocity,  $U^*$ , thickness of the logarithmic region,  $\delta_{\text{log}}$ , as well as the Reynolds numbers based on these quantities – are listed in Table 3 for the various free stream velocities. These characteristics are close to the values expected from the theory.

As mentioned in Section 2.2, the study of the bubble motion was performed for bubbles with diameters between

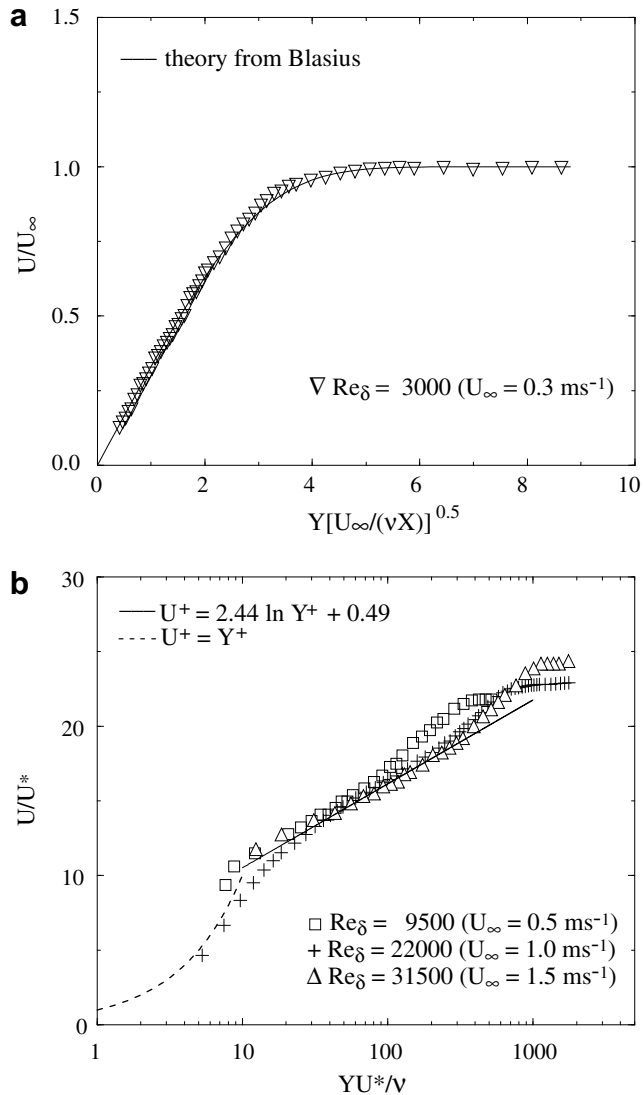


Fig. 3. Dimensionless liquid velocity profiles at  $X = 1$  m under single-phase flow conditions: (a) laminar flow; (b) turbulent flow.

Table 3  
Boundary-layer flow parameters at  $X = 1$  m

$U_\infty$ (m s $^{-1}$ )	$U^*$ (m s $^{-1}$ )	$\delta$ (mm)	$\theta$ (mm)	$\delta_{\text{log}}$ (mm)	$G_{\text{log}}^{\text{a}}$ (s $^{-1}$ )	$\delta^{+\text{b}}$	$Re_X$	$Re_\delta$	$Re_\theta$
0.3	0.007	10	0.1	–	–	5.5	$3 \times 10^5$	3000	290
0.5	0.023	19	1.8	3.5	27	437	$5 \times 10^5$	9500	920
1.0	0.044	22	2.1	4.5	62	968	$1 \times 10^6$	22,000	2140
1.5	0.062	20	1.9	4.0	106	1240	$1.5 \times 10^6$	30,000	2920

<sup>a</sup>  $G_{\text{log}}$  denotes the mean velocity gradient in the logarithmic region.

<sup>b</sup>  $\delta^+$  is the boundary layer thickness in wall units except for laminar conditions ( $U_\infty = 0.3 \text{ m s}^{-1}$ ), where it is defined as  $\delta/(U_\infty/\nu_L X)^{0.5}$ .

2 mm and 6 mm. In quiescent contaminated water (Clift et al., 1978), this diameter range corresponds schematically to two families of shape and motion: ellipsoidal bubbles whose trajectories are principally helical ( $2 \text{ mm} \leq d_{\text{eq}} \leq 4 \text{ mm}$ ;  $1.7 \leq We \leq 3.4$ ) and highly deformable bubbles with almost rectilinear rocking motions ( $d_{\text{eq}} \geq 4 \text{ mm}$ ;  $We \geq 3.4$ ). To specify the initial conditions, the bubble distribution was measured with the optical probe at the inlet of the visualization area, as a function of the bubble diameter. Fig. 4a shows representative results obtained for 3 mm diameter and  $U_\infty = 1.0 \text{ m s}^{-1}$ . We see that starting from the injection point ( $X_{\text{inj}} = 0.3 \text{ m}$ ,  $Y_{\text{inj}} = 0.7\delta$ ), the bubbles disperse well in the free stream before reaching the working section. The resulting distribution is roughly Gaussian and bubbles penetrate in the boundary layer by the outer edge, so that the flow disturbances caused upstream are limited. The same trends were found for the other diameters, with however, a smaller lateral dispersion for the largest diameters (see Table 1). This is essentially due to the intrinsic bubble path which changes from oscillating into rocking.

### 3.2. Bubble migration: the results for $1.0 \text{ m s}^{-1}$ free stream velocity

Bubble motion was first investigated for a constant free stream velocity of  $1.0 \text{ m s}^{-1}$  ( $Re_\delta = 22,000$ ) and all the bubble diameters. Fig. 4b provides samples of raw trajectories obtained for 2 mm diameter bubbles, which illustrate the phenomenon of migration. Two populations of bubbles with different types of trajectories are clearly distinguishable. In the free stream, bubbles are rising with an oscillating path, parallel to the plate and qualitatively comparable to the path observed in quiescent water for the same diameter. Inside the boundary layer, the oscillating motion is amplified, less regular both in period and direction and sometimes transforms into a sudden deflection towards the plate. In the example marked with the open white circles, the deflection starts near the outer edge and drives the bubble into contact with the plate, where it remains trapped and slides along the surface. The trajectory of another bubble sliding along the surface is shown marked

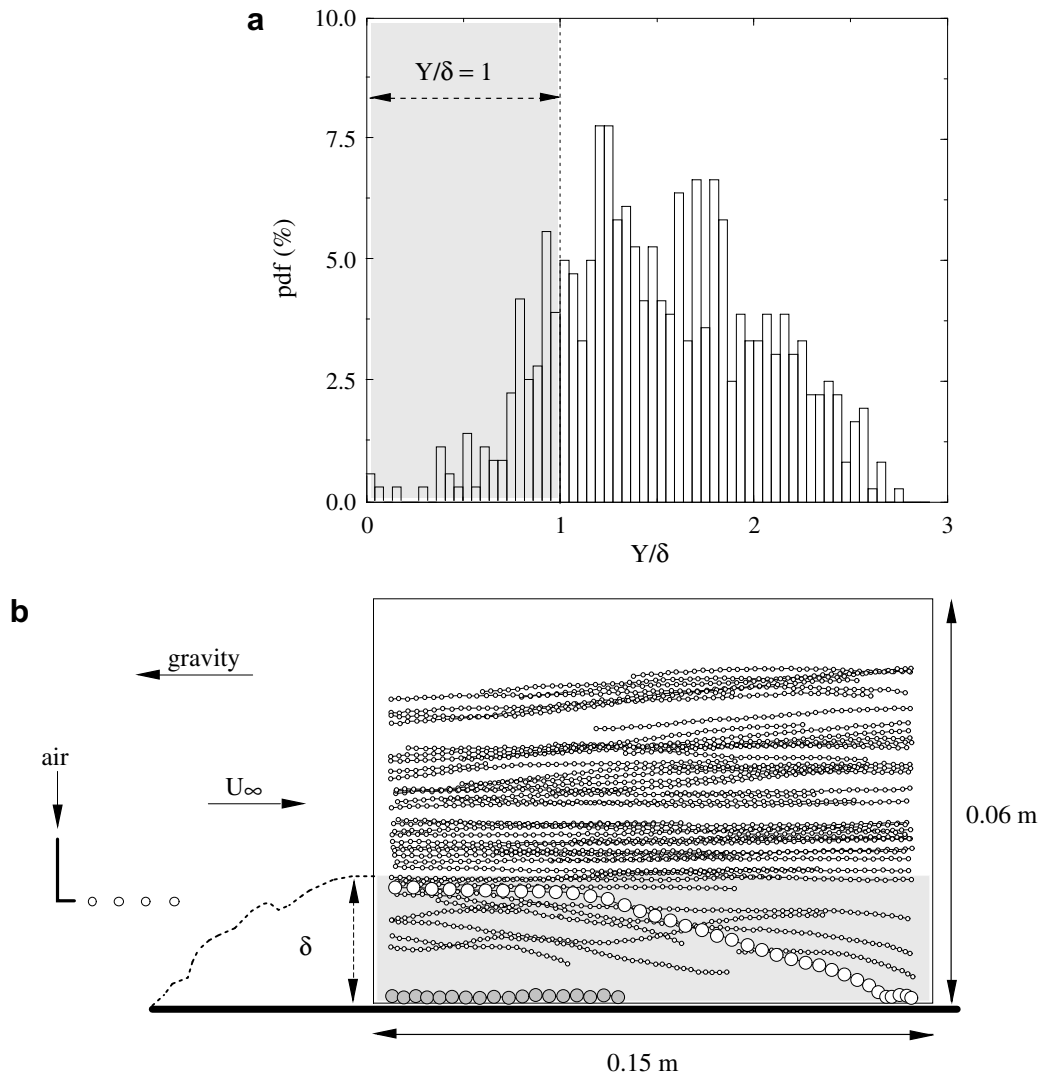


Fig. 4. (a) Representative distribution of 3 mm bubbles at the entrance to the working section  $X = 1 \text{ m}$ ; (b) an example of trajectories of 2 mm bubbles showing a migrating bubble.  $U_\infty = 1 \text{ m s}^{-1}$ .



with open grey circles. This sequence of deflection followed by trapping essentially characterizes the phenomenon of bubble migration.

Samples of typical raw trajectories obtained for the other diameters can be found in Tran-Cong et al. (1998) and Tran-Cong (1999). A probabilistic analysis of hundreds of such trajectories shows that the migration: (i) only takes place inside the boundary layer, (ii) only occurs for small bubble diameters up to 3.5 mm, and (iii) only occurs for 15–25% of the bubbles, indicating that it is non-systematic. Bubbles larger than 4 mm still approach the plate quite closely, but they are not trapped at the wall and they return to the flow. The critical diameter for transition between these two types of behaviours,  $3.5 \text{ mm} < d_{\text{eqcrit}} < 4 \text{ mm}$ , is similar to the values reported in other studies of pipe and channel flows (Sekoguchi et al., 1979; Zun, 1988; Liu, 1993). To obtain a better insight into the influence of bubble size we have constructed composite images showing time sequences of bubble shape and bubble position as the bubble moves towards the plate. Typical sequences for bubbles with diameters of 2–3.5 mm and 4–6 mm are shown in Fig. 5, from which we can see clearly that the change of behaviour observed above 4 mm concerns both trajectory and bubble shape.

For bubble diameters between 2 mm and 3.5 mm, the deflection is, on average, accentuated and as bubbles approach the wall their shape remains approximately ellipsoidal, with the major axis inclined at an angle of about  $45^\circ$  to the  $X$  axis. This direction turns out to be one of the principal axes of the straining motion in the shear. Bubbles then penetrate entirely into the region of high shear (logarithmic and buffer regions), become elongated as they touch the surface, rotate and finally slide along the surface, where they progressively recover a stable, inclined ‘pear’ shape. This shape, characteristic of the sliding motion, was documented in detail by Sekoguchi et al. (1974) and Sato et al. (1976) in channel flow. These authors measured the thickness of the liquid film between the bubble and the surface and found it to be of the order of 30–40  $\mu\text{m}$ , showing that the bubble surface closest to the wall is embedded in the vis-

cous sub-layer. The formation of this liquid film is important, because it explains the stable sliding motion of the bubbles and why the trapped bubbles move more slowly. Bubbles with diameter greater than 4 mm behave quite differently. They do not really move towards the wall in a deterministic sense, but from time to time the natural lateral motion in their trajectories carries them close to the wall, at which point they become distorted and appear to ‘reach’ towards it. But because of their size, they are never fully immersed in the region of high shear. As the bubble interface approaches the wall, it is strongly stretched at an angle of approximately  $45^\circ$ , to form a tip with a small curvature which comes into contact with the plate. The stretching intensifies during the contact with the surface, then the tip detaches; trapping does not take place. In a number of cases, a capillary wave is generated, propagates clockwise around the bubble and contributes to the destruction of the wall contact (Nikitopoulos et al., 2004). After detachment, the interface relaxes and the bubbles return to the flow. The shape of the bubbles as they impact on the plate is rather similar to that of an airfoil, oriented in the shear direction. Kariyasaki (1987) reported the same type of deformation for bubbles submitted to a linear shear in a laminar flow. Using classical wing theory, he showed that such deformation leads to an inversion of the lift force towards the region of higher velocity. More sophisticated numerical simulations based on interface tracking methods (Ervin and Tryggvason, 1997; Tomiyama et al., 1995) provide evidence that this lift reversal is associated with a change in the net flow circulation around the bubbles resulting from the interaction of the distorted interface with the local shear. A similar effect might be induced here by the high shear in the wall region, which would also contribute to the departure of the bubble. But the departure could also simply result from entrainment by the outer flow, since more than half the bubble remains outside the region of high shear, where it is subjected to a high drag force from the external flow.

Complementary information on the trapping process was obtained by measuring the rate of bubbles that come into contact with the plate, as a function of the injection distance

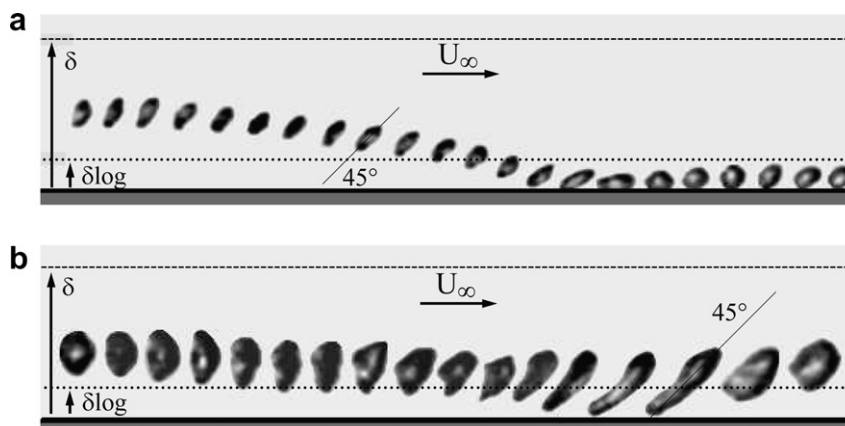


Fig. 5. Bubble pictures at different stages in their motion towards the plate. (a)  $d_{\text{eq}} = 3 \text{ mm}$ , trapping; (b)  $d_{\text{eq}} = 6 \text{ mm}$ , no trapping.

$Y_{inj}$  and the equivalent diameter (Section 2.3, Fig. 1b). The results are plotted in Fig. 6. When the bubbles are released at the surface ( $Y_{inj} = d_{eq}/2$ ), the rate is found equal to unity for bubbles up to 3.5 mm in diameter and only 0.5 for larger bubbles, which signifies that all the small bubbles injected remain sliding in a stable motion, whilst the large bubbles progressively escape from the plate. So the value previously obtained for the critical diameter for bubble movement to the wall corresponds to the critical value observed for trapping bubbles at the wall. We conclude from this that the critical migration value arises from the impossibility of trapping large bubbles at the wall, rather than from an inability of the large bubbles come close to the wall. These findings are in agreement with stroboscopic visualizations of Sekoguchi et al. (1979), who observed a similar transition for bubbles with major axis between 4 mm and 5 mm. Here, the critical diameter is of the same order as the thickness of the logarithmic layer  $\delta_{log}$  (see Table 3). To check that the wake of the nozzle had no influence on the results, we also performed some experiments in which bubbles were released directly from a hole in the plate (Tran-Cong, 1999). They yielded the same trends and confirmed that the departure of large bubbles from the wall was linked to significant distortion of the interface, leading to destruction of the surface contact. The behaviour exhibited in Fig. 6 at  $Y_{inj} = d_{eq}/2$ , persists up to the injection distance  $Y_{inj} = \delta_{log}$ , indicating that the small bubbles released in the high shear region all come into contact with the wall and are captured. As the distance increases further, the rate of wall contacts decreases, because deflections towards the plate become non-systematic. We see that the deflections vanish at  $Y_{inj} = \delta$  for the small diameters and around  $\delta/2$  for the large diameters, in agreement with the trends illustrated by the trajectories in Fig. 7.

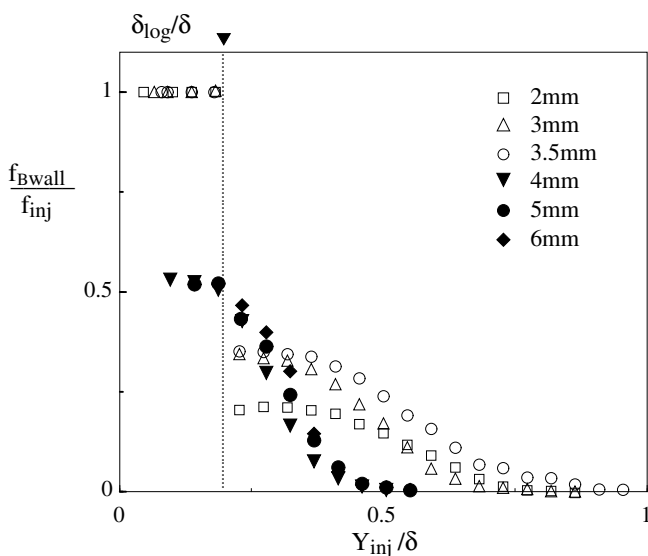


Fig. 6. Rate of bubbles trapped at the wall as a function of the mean equivalent bubble diameter and the injection distance scale by  $\delta$ .  $U_\infty = 1 \text{ m s}^{-1}$ .

The trajectories of the migrating bubbles were analysed further by plotting together all the migration trajectories that reached the wall, for a given bubble diameter. The impingement point for each trajectory was shifted to a common origin ( $X = 0$ ) to demonstrate the universal nature of the migration trajectories in the near wall region. This is illustrated by Fig. 7, for 2, 3.5 and 4 mm diameter bubbles. Plotted in this way, the transition between 3.5 and 4 mm is particularly evident. Bubbles larger than 4 mm are never captured at the wall, and their trajectories towards the surface resemble more the oscillating paths of bubbles rising close to a wall, than true deflections towards it. For small bubbles, the interesting points are that: (i) the deflections towards the plate follow non-deterministic trajectories in the sense that they differ significantly from one bubble to another, (ii) a significant number of the deflected trajectories start abruptly near the edge of the boundary layer, where the mean shear is very weak, with a strong acceleration towards the plate and (iii) the typical time scale of the migration phenomena is short – around 0.12 s. These observations all suggest that the mean shear-induced lift-force cannot provide the driving force towards the wall in this part of the flow. This conclusion is confirmed by the detailed analysis of bubble trajectories presented later in Section 3.3 which shows that the mean shear-induced lift force calculated with available lift coefficient models is far too small to reproduce quantitatively the mean trajectories of migrating bubbles. This is particularly true at the outer edge of the boundary layer, where the shear is the weakest (typically of the order of  $2 \text{ s}^{-1}$ ) and the lateral acceleration of the bubble is the strongest. We note that, on average, the deflections of 3.5 mm bubbles start closer to the wall than for 2 mm bubbles and are less accentuated, reflecting a lower momentum towards the plate. In some cases, such as those trajectories shown in black in Fig. 8, bubbles are deflected sufficiently strongly to enable them to reach the wall, but they do not penetrate inside the shear layer and finally return to the flow. Examination of the corresponding videos shows that some of these wall evictions are caused by the presence of bubbles already sliding along the surface, but this is not systematic and other mechanisms are probably involved. The fact that bubbles are only captured at the wall if they penetrate the region of high shear corroborates the previous measurements of the trapping rate (Fig. 6). It supports the idea that migration might result from the combination of two mechanisms: one which drives bubbles close to the inner layer and another which traps them inside. The lift force induced by the high mean shear in the surface layer seems to be the most plausible explanation for the end of deflection and trapping. A force-type potential associated with the bubble image (Milne-Thomson, 1968) might also contribute to the process, but this will attract bubbles to the wall whatever the flow direction, so it alone cannot explain the fact that no sliding bubbles are observed in downward flow (Sekoguchi et al., 1979; Kashinsky and Randin, 1999). Hence, the thickness of the high shear region relative to the bubble diameter is

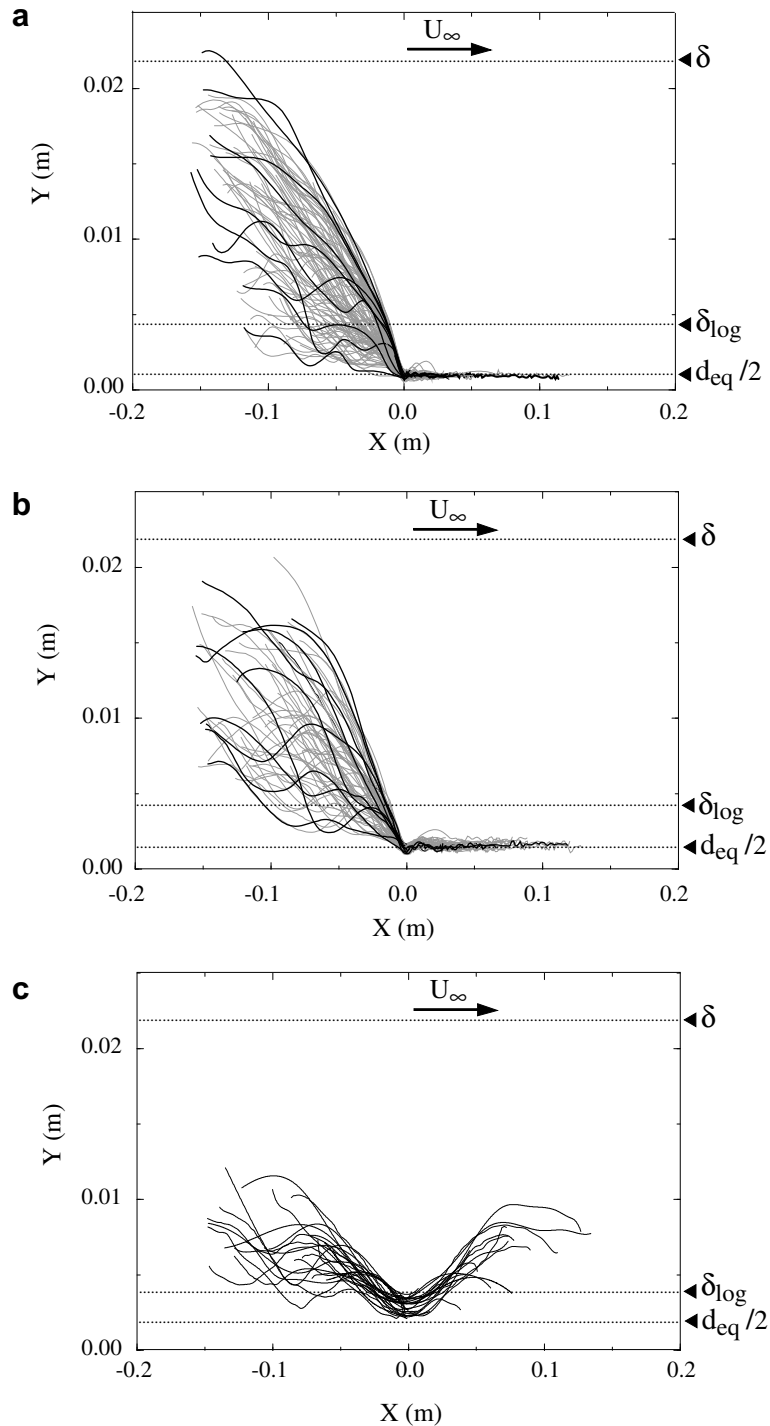


Fig. 7. Trajectories of bubbles that come into contact with the wall; all the impingement points have been shifted to the same origin  $X = 0$ .  $U_\infty = 1 \text{ m s}^{-1}$ , (a)  $d_{\text{eq}} = 2 \text{ mm}$ , (b)  $d_{\text{eq}} = 3.5 \text{ mm}$ , (c)  $d_{\text{eq}} = 4 \text{ mm}$ . Migration time scale: 0.12 s.

probably an important parameter determining the trapping and could explain the existence of a critical size.

Since the migrations have this above mentioned ‘non-deterministic’ character and a short time scale, one might reasonably expect that the turbulence in the outer layer should play a significant role in driving bubbles towards the wall. This question was first examined by comparing the amplitude  $A_i$  of the lateral oscillations of the bubbles ris-

ing inside the boundary layer without contact with the wall and outside the boundary layer, for different diameters. The maximum value of the amplitude was measured for each trajectory and plotted as a function of the mean bubble distance from the wall, scaled by the boundary layer thickness  $\delta$ . The data exhibit two main trends according to the diameter range. In the range 2–3.5 mm (Fig. 9a), the amplitudes of the oscillations inside the boundary layer

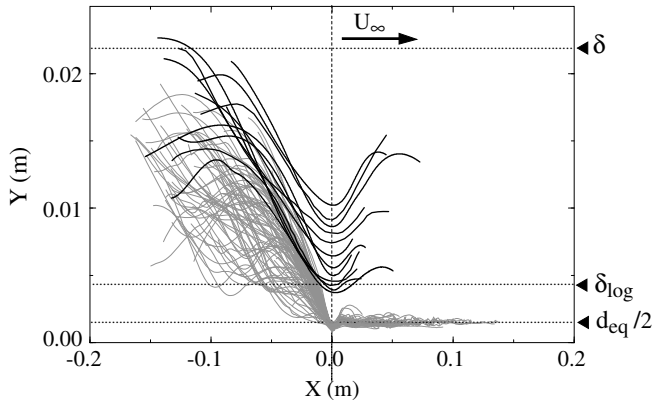


Fig. 8. Some trajectories (in black) showing strong deflections without trapping at the wall.  $U_\infty = 1 \text{ m s}^{-1}$ ;  $d_{eq} = 3 \text{ mm}$ .

are, on average, twice as high as those outside the boundary layer, and vary strongly from one trajectory to another near the wall. The standard deviation there is about twice that in the free stream. Rather surprisingly, the amplitudes pass through a minimum at the edge of the boundary. The reason for this latter point remains unclear. In contrast, for bubbles above 4 mm (Fig. 9b), the amplitudes of the oscillations do not change significantly between the inner and outer regions. These results suggest that the bubbles which are most affected by the turbulent fluctuations in the boundary

layer are the small ones with diameters up to 3.5 mm, and this is precisely the diameter range for which migration towards the wall is observed. A few additional runs (Tran-Cong, 1999; Tran-Cong et al., 1998) were performed with 1 mm spherical bubbles: Stokes number  $\sim 0.3$ , Weber number  $\sim 0.2$ , which had a quasi rectilinear motion in the free-stream and small drift velocity  $\sim 0.1 \text{ m s}^{-1}$ . They showed that the lateral displacements generated by the wall-normal fluctuations were weak compared with those for bubble diameters of 2–3.5 mm diameters ( $A_i < 4 \text{ mm}$ ) and that the migration rate was in this case very low: 3%. The unsteady helical motion seems therefore more ‘easily destabilized’ inside the boundary layer and yields a higher migration rate, in agreement with the observations of Zun (1988).

Next step was to investigate the influence of the flow regime on the migration and to clarify the possible effect of bubble–bubble interactions.

### 3.3. Influence of the flow regime and bubble–bubble interactions

Bubble trajectories were measured for three other free stream velocities (Table 2), one in the laminar regime ( $U_\infty = 0.3 \text{ m s}^{-1}$ ), the others in post-transition ( $U_\infty = 0.5 \text{ m s}^{-1}$ ) and turbulent regimes ( $U_\infty = 1.5 \text{ m s}^{-1}$ ). The rate of migration inferred from these trajectories and defined

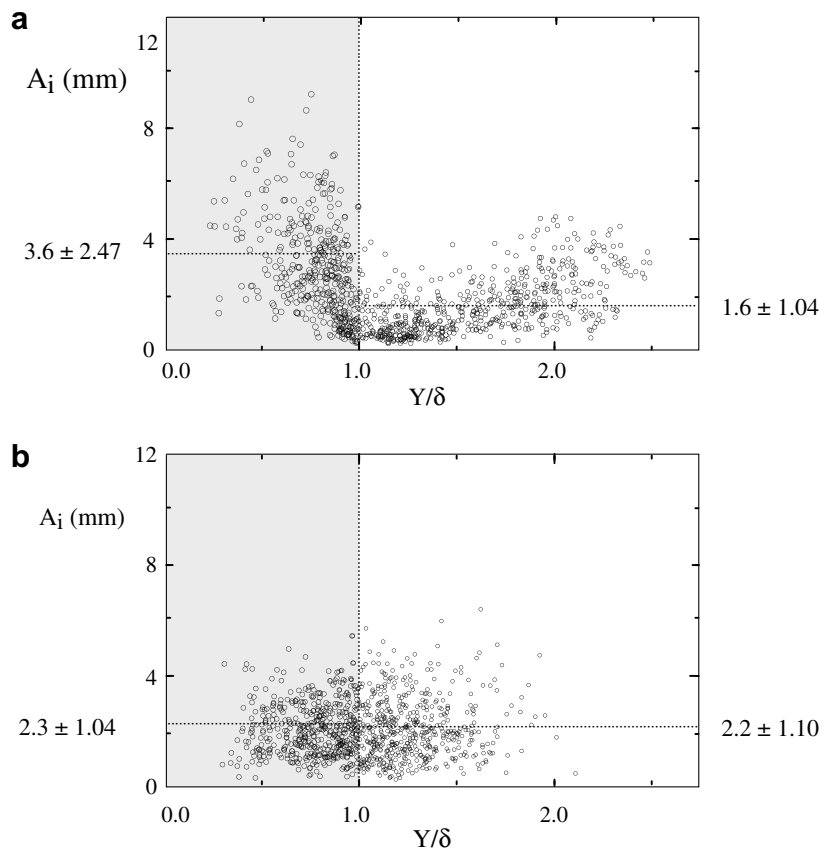


Fig. 9. Amplitude of the lateral oscillations for the bubbles inside and outside the boundary layer. (a)  $d_{eq} = 2 \text{ mm}$ , (b)  $d_{eq} = 6 \text{ mm}$ . ..... Average value and standard deviation per zone.

as the number of migrations divided by the number of bubbles rising in the boundary layer, is plotted in Fig. 10 versus the Reynolds number based on the momentum thickness  $Re_\theta$ . As can be seen, no migration occurs in laminar regime. In these experiments, the trajectories show that a few bubbles come into contact with the wall, but after several rebounds of decreasing amplitude, they return to the flow: there is no trapping at the wall (Tran-Cong, 1999; Tran-Cong et al., 2001). Similar behaviour in bubbly channel flow was reported by Sekoguchi et al. (1979) who found that migrations disappeared below  $0.3 \text{ m s}^{-1}$ , to be replaced by a ‘hopping’ (or ‘bouncing’) motion. Unfortunately they did not specify whether this resulted from a change in the flow regime. Other experiments have shown evidence of bubble migration in laminar pipe flows (Kashinsky et al., 1993), but these experiments tended to be performed in configurations with much higher bubble lift forces. The absence of bubble migration in our experiments might therefore be the result of the low shear in the relatively thin boundary layer. The results in Fig. 10 show clearly that in these experiments, bubbles only migrate as the boundary layer becomes turbulent. The rate of migration starts from zero in laminar flow, rises rapidly up to 10% after the transition, and continues to increase with  $Re_\theta$ , as the turbulence in the boundary layer increases further. These results are consistent with the previous Eulerian measurements of Moursali et al. (1995), who noted that the number of bubbles sliding along the plate increased with increasing free-stream velocity. One particularity of the migrations at  $0.5 \text{ m s}^{-1}$  is that the trapping is not always immediate. In some cases (amounting to 2–3% of the measured trajectories) bubbles impact on the plate and then bounce once or twice before becoming trapped and sliding

along the surface (Tran-Cong, 1999). This behaviour, which tends to vanish at higher Reynolds numbers, is consistent with the idea that a shear-induced lift force might contribute to the trapping. At low Reynolds number, the shear at the wall is relatively weak, so the shear-induced lift force is also weak, and cannot balance the repulsive force generated by the impact of the bubble at the surface. The simplified 1D model proposed very recently by Zaruba et al. (2007) to explain the bouncing of single bubbles on a flat wall in a vertical square duct tends to confirm this explanation. For all values of  $Re_\theta$ , the migration rate is a maximum for bubble diameters in the range 2–3 mm, decreases for 3.5 mm diameter bubbles and drops to zero for bubble diameters greater than 4 mm. This shows that the critical diameter does not change over the range of Reynolds numbers used in these investigations. The fact that the thickness of the high shear region remains sensibly constant and greater than 3.5 mm over that range (see Table 3), could explain why the critical diameter for sliding bubbles remains independent of Reynolds number.

The influence of the Reynolds number on bubble migration was quantified more precisely by comparing the average trajectory for the migrating bubbles. This was done by computing the average of 100 migration trajectories, for each combination of bubble diameter and free stream velocity. For each trajectory the time base and the coordinates  $(X_n(t_n), Y_n(t_n))$  were adjusted relative to the instant  $T_n$  and the position  $(X_n^o, Y_n^o)$  at which the bubble reached the wall. Then the coordinates  $(\bar{X}(t_i), \bar{Y}(t_i))$  of the average trajectory are given by:

$$\bar{X}(t_i) = \frac{1}{N_i} \sum_{n=1}^{n=N_i} [X_n(t_i + T_n) - X_n^o],$$

$$\bar{Y}(t_i) = \frac{1}{N_i} \sum_{n=1}^{n=N_i} [Y_n(t_i + T_n) - Y_n^o] \quad (1)$$

where  $N_i$  is the number of bubble positions averaged at instant  $t_i$ . The duration of the migration varies from one bubble to another, so the deflections do not all start at the same time, relative to the instant at which the bubbles reach the wall. The first part of the average trajectory is therefore computed from an average over a relatively small number of bubbles, and this increases as the bubbles reach the wall. The instantaneous mean longitudinal and transversal migration velocities  $U_B(t), V_B(t)$  were derived by differentiating the average trajectory. The average bubble coordinates  $\bar{X}(t)$  and  $\bar{Y}(t)$  are plotted as functions of time in Fig. 11a, b; the average trajectories themselves are shown in Fig. 12 and the velocities are plotted in Fig. 13a and b. Fig. 11b shows that, on average, the migration of the 2 mm bubbles begins farther from the wall ( $Y \sim 0.7\delta$ ) than for the bubbles with diameters in the range 3–3.5 mm ( $Y \sim 0.5\delta$ ). Their migration is also more rapid, except for a free stream velocity of  $0.5 \text{ m s}^{-1}$ , for which all bubbles have the same migration velocity. Interestingly, the bubble trajectories in the region  $0 < Y \leq 0.3\delta$  are the same for all bubble diameters,

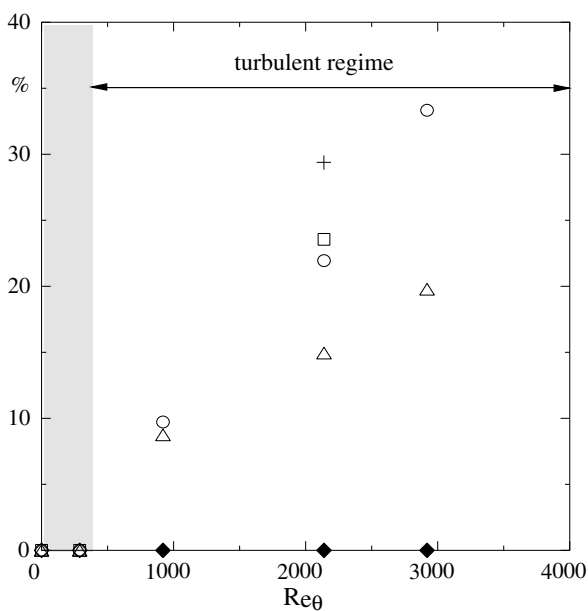


Fig. 10. Rate of migration vs Reynolds number based on momentum thickness: (○)  $d_{eq} = 2 \text{ mm}$ ; (□)  $d_{eq} = 3 \text{ mm}$ ; (△)  $d_{eq} = 3.5 \text{ mm}$ ; (◆)  $d_{eq} = 4 \text{ mm}$ ; (+)  $d_{eq} = 3 \text{ mm SB}$ .

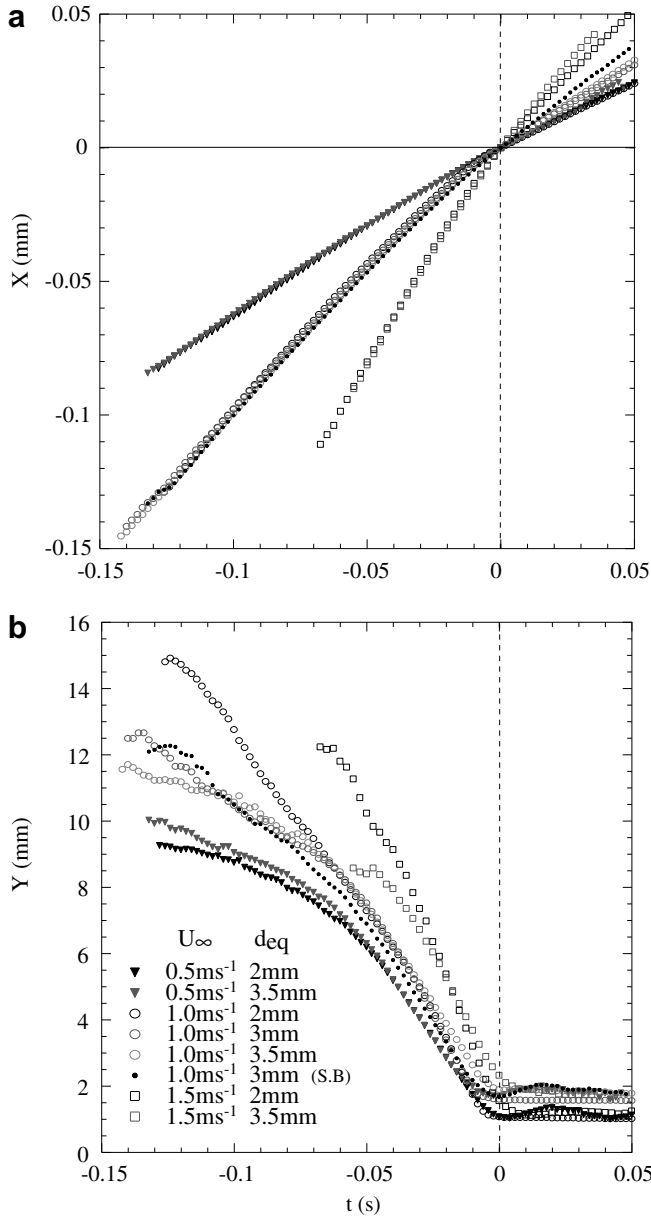


Fig. 11. Mean coordinates of Lagrangian trajectories of migration vs time for different free stream velocities and bubble equivalent diameters. (SB) = single bubble case.

and for all values of the free stream velocity. This suggests that the driving forces in the near wall region are similar for all bubble types and flow conditions. This is the region of the flow where bubbles approaching the logarithmic layer decelerate in the streamwise direction and accelerate towards the wall (Fig. 13a and b), before impacting on the surface. The average transverse and streamwise migration velocities for the different experimental conditions are presented in Table 4. These results show that the transverse velocity  $V_B(t)$  increases with the Reynolds number, so the characteristic time for bubble migration drops from 0.14 s at  $U_\infty = 0.5 \text{ m s}^{-1}$  to 0.07 s at  $U_\infty = 1.5 \text{ m s}^{-1}$ . This increase in  $V_B(t)$  with increasing Reynolds number is consistent with the idea that the migration is driven by a

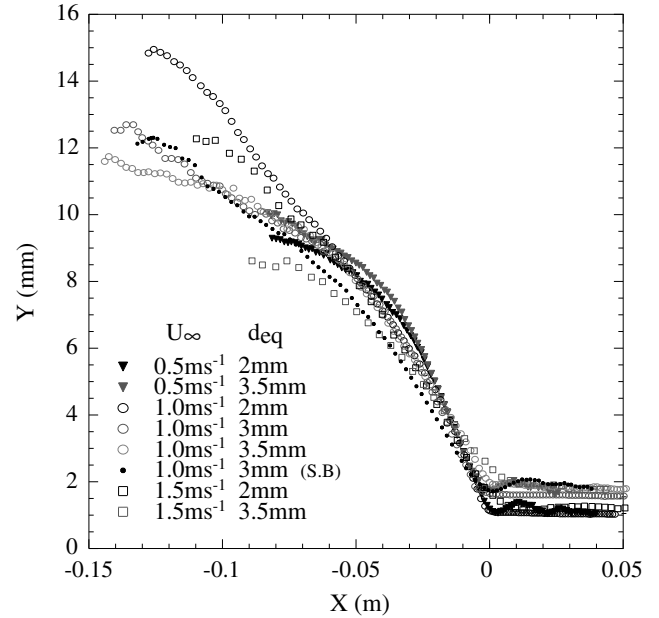


Fig. 12. Mean Lagrangian trajectories of migration vs streamwise coordinate for different free stream velocities and bubble equivalent diameters. (SB) = single bubble case.

shear-induced lift force; as the Reynolds number increases, so does the shear, and the shear-induced lift force, and so the bubbles migrate towards the wall more rapidly. Of course, this explanation can only really be valid for bubble motion in the near-wall region, where the velocity gradients are high; it cannot explain events further out where the velocity gradient changes rather slowly with Reynolds number.

To test whether the shear-induced lift force is capable of driving bubble migration similar to that observed in these experiments, Tran-Cong et al. (1998) compared the measured trajectory of a 2 mm diameter bubble rising in a boundary layer with a free stream velocity of  $1 \text{ m s}^{-1}$  with the theoretical trajectory obtained by integrating the equation of motion for a spherical bubble at high Reynolds number (Auton et al., 1988). The drag coefficient was computed from the empirical relationship  $C_D = (24/Re_B)(1 + 0.15Re_B^{0.687})$  (Schiller and Nauman, 1933), and the added mass and lift coefficients were both taken equal to 0.5. The wall-normal profile of the average streamwise velocity was assumed to be logarithmic. The measured and theoretical profiles have both been plotted in Fig. 13a and b, from which it can be seen that the measured migration velocity  $V_B(t)$  is much greater than the theoretical velocity. To investigate this difference, the theoretical trajectory was recalculated, adjusting the values of the drag and lift coefficients at each time step so as to maximise agreement with the measured trajectory; the added mass coefficient was kept constant at its original value of 0.5. The optimised value of  $C_D$  remained almost constant over the whole trajectory, and very close to the theoretical value given by the correlation of Schiller and Nauman (1933), except close to the wall, whereas the inferred values of  $C_L$  were up to 6 or 7 times

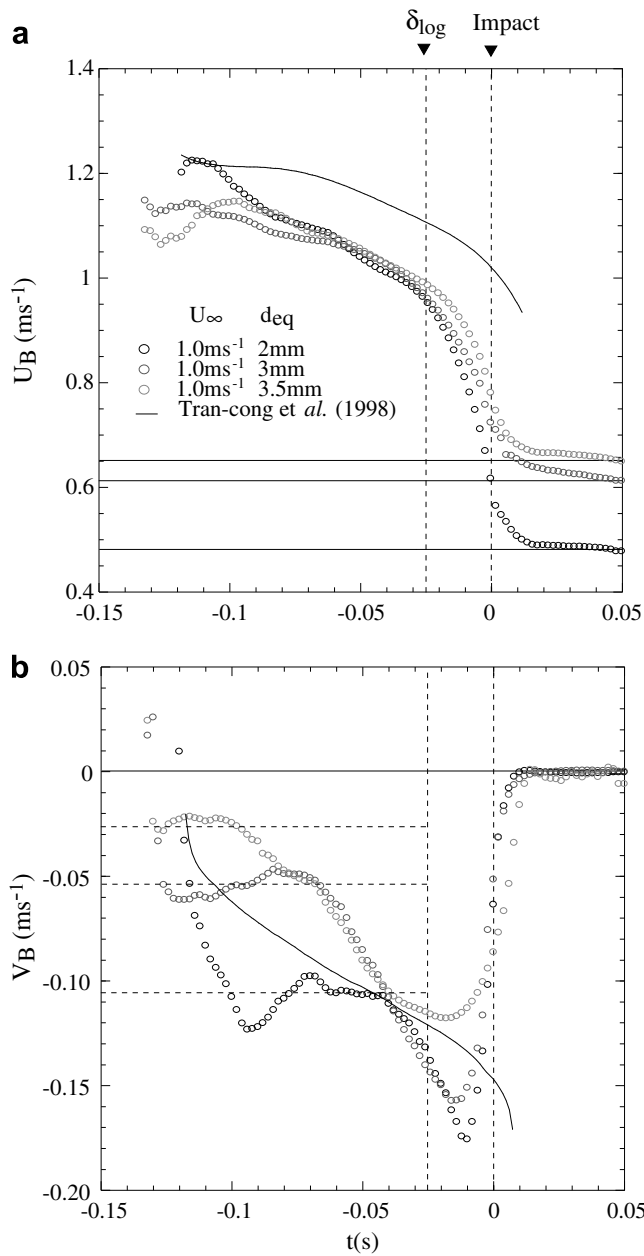


Fig. 13. Mean longitudinal (a) and transversal (b) bubble migration velocities.  $U_\infty = 1 \text{ m s}^{-1}$ . — Theoretical prediction for 2 mm bubble diameter.

greater than the inviscid value in the outer layer, and 2–4 times greater near the wall. One possible explanation for the observed increase in migration velocity is that the lift coefficient is modified by the shear-induced deformation of

the bubble and its wake; this is certainly plausible when the bubble is close to the wall, where the shear is strong, and the blockage effect of the wall is important, but it is unlikely to be a significant effect in the outer layer, where the apparent increase in  $C_L$  is greatest. Another possible explanation is that the migration in the outer layer is driven by large scale intermittent turbulent structures; these should have most influence on bubble migration when the bubble is far from the wall, and their influence should decrease as the bubble approaches the wall, because of the blocking effect of the wall. This is consistent with the variation in the effective value of  $C_L$  inferred from the computed trajectory.

Bubble–bubble interactions could also influence migration velocities, so to investigate this effect some experiments were performed in which 3 mm diameter bubbles were released individually from the injector, in a flow with a free stream velocity of  $1 \text{ m s}^{-1}$ . The migration trajectories of these isolated bubbles have also been plotted in Figs. 11 and 12, together with those for continuous injection, and there is no significant difference between the two conditions. The migration rate for the isolated bubbles was slightly higher (30%) than the rate measured for continuous release (25%), but this observation should be treated with caution, since it based on relatively few isolated bubble trajectories (about 100 trajectories in total). Further details of this comparison are provided in Tran-Cong (1999) and Tran-Cong et al. (2001). So it seems reasonable to conclude bubble–bubble interactions do not influence the dynamics of bubble migration, but they might possibly reduce the overall migration rate. This also confirms that two-way coupling is not an important effect for the dilute conditions studied here.

### 3.4. Role of the large scale turbulent structures

In order to investigate the influence of large scale turbulent structures on bubble migration, we have carried out some flow visualization experiments, at free stream velocities of  $U_\infty = 0.5 \text{ m s}^{-1}$  and  $U_\infty = 1 \text{ m s}^{-1}$ . The general technique is described in detail in Section 2.3; in essence, the intermittent structure of the boundary layer is visualised by injecting Rhodamine B dye at the wall, and illuminating a slice of the flow normal to the wall, using a laser light sheet. The dye diffuses through the boundary layer, and fluoresces in the laser light, so that the large scale structures appear as a succession of turbulent ‘bulges’ whose outer edges define the instantaneous limit of the boundary layer. The bubble trajectories and turbulent structures were filmed

Table 4  
Mean longitudinal and transversal bubble migration velocities

$U_\infty$ (m s <sup>-1</sup> )	$d_{\text{eq}} = 2 \text{ mm}$		$d_{\text{eq}} = 3 \text{ mm}$		$d_{\text{eq}} = 3 \text{ mm (S.B)}$		$d_{\text{eq}} = 3.5 \text{ mm}$	
	$U_B$ (m s <sup>-1</sup> )	$V_B$ (m s <sup>-1</sup> )	$U_B$ (m s <sup>-1</sup> )	$V_B$ (m s <sup>-1</sup> )	$U_B$ (m s <sup>-1</sup> )	$V_B$ (m s <sup>-1</sup> )	$U_B$ (m s <sup>-1</sup> )	$V_B$ (m s <sup>-1</sup> )
0.5	0.641	−0.062	0.640	−0.063	–	–	–	–
1.0	1.036	−0.111	1.024	−0.080	1.009	−0.0781	1.036	−0.067
1.5	1.624	−0.154	–	–	–	–	1.639	−0.113

using high speed cameras (see Table 2), with a framing rate high enough to enable us to follow individual bubbles as they migrated, for both the free stream velocities. Fig. 14a and b shows some typical time sequences illustrating the evolution of these structures. The bubbles in the boundary layer appear as bright white spots, but not all such bubbles are located within the light sheet; the bubbles actually in the light sheet block the light from the laser (through internal reflections within the bubble) so that there is a shadow

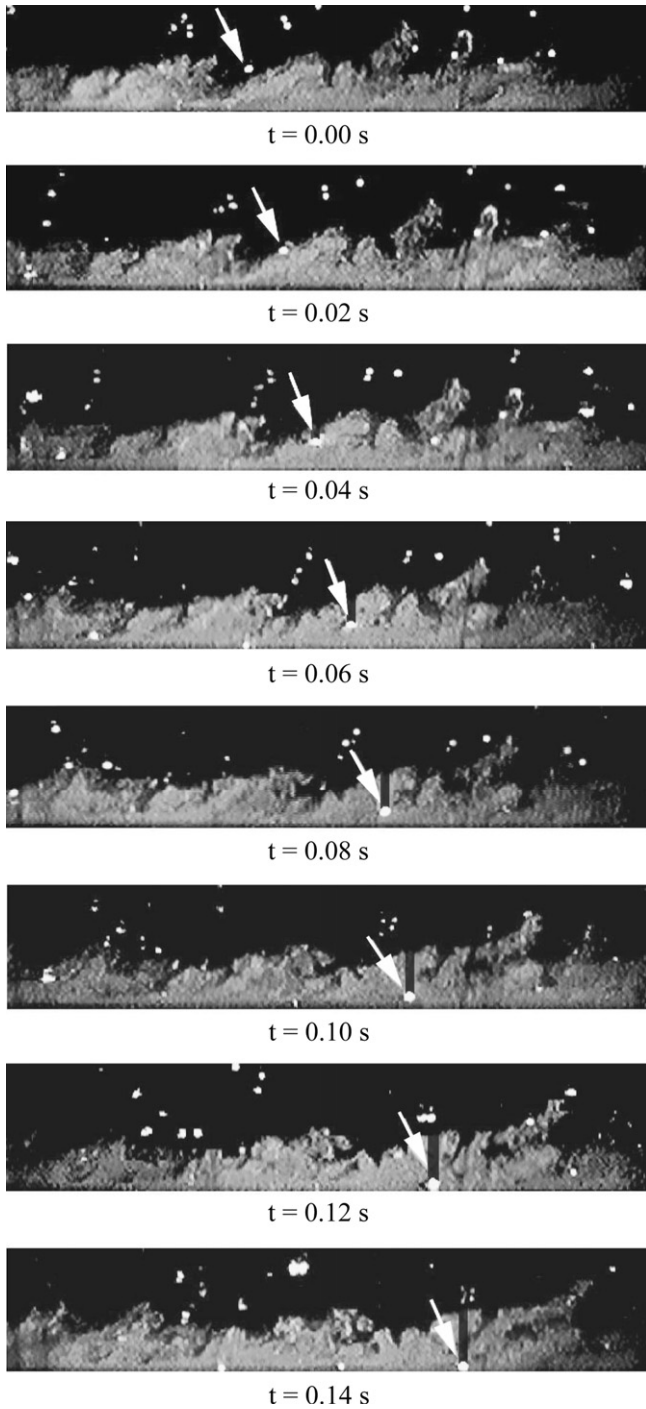


Fig. 14a. A time sequence showing the migration of a bubble in a large scale turbulent structure.  $U_\infty = 0.5 \text{ m s}^{-1}$ ;  $d_{eq} = 3 \text{ mm}$ .

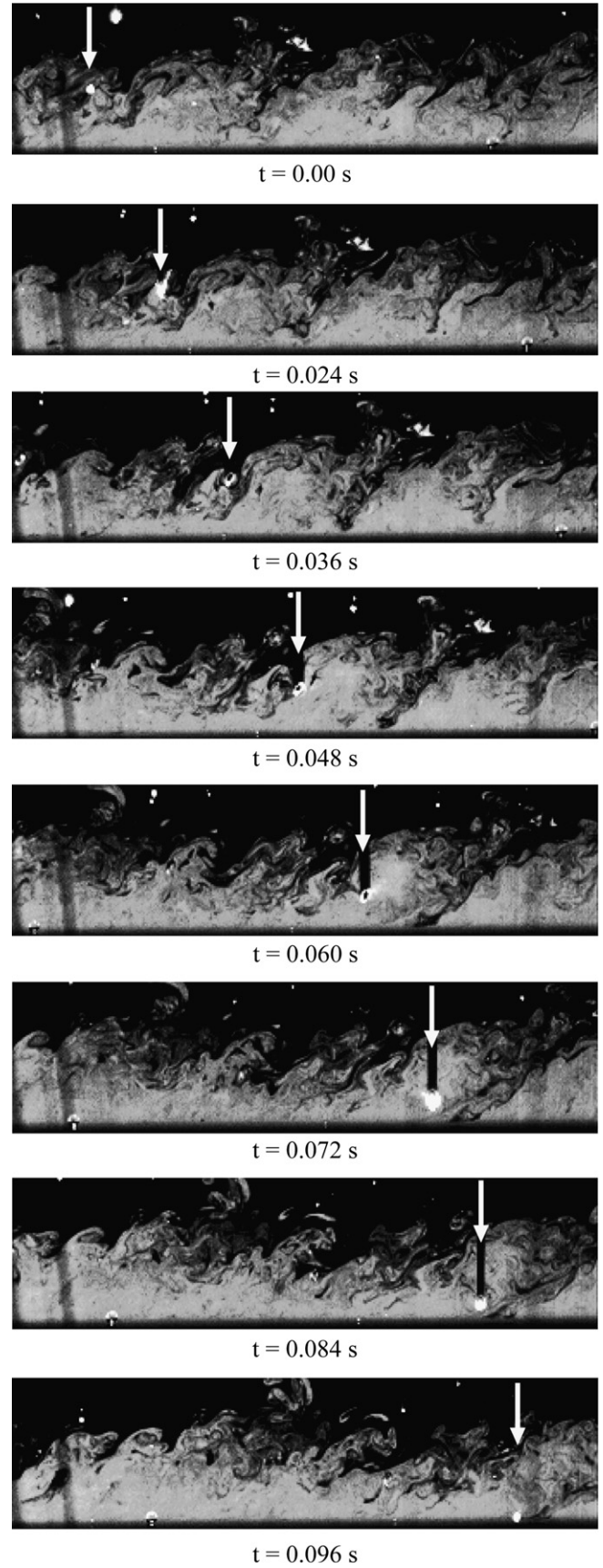


Fig. 14b. A time sequence showing the migration of a bubble in a large scale turbulent structure.  $U_\infty = 1 \text{ m s}^{-1}$ ;  $d_{eq} = 2 \text{ mm}$ .



region behind them, and we have used the presence or absence of this shadow region to discriminate between the bubbles in the light sheet and those outside it. This is important, because the bubble trajectories are three-dimensional, as are the structures themselves, so the fact that a bubble image occurs inside a structure does not of itself guarantee that the bubble is physically located within the structure. In total we filmed 25 such sequences, each lasting 5.452 s, from which we obtained 455 migration trajectories, for bubbles which remained within the light sheet throughout the duration of their migration, and the statistics presented here are based only on those trajectories.

These intermittent turbulent structures have been studied by many researchers, and detailed descriptions of their properties can be found in Kovanay et al. (1970), Head and Bandhyopadhyay (1981) and Robinson (1991), for example. Here we simply summarise the characteristics that seem to be most relevant to the migration of bubbles across the boundary layer. The bulges are three-dimensional, with characteristic length scales in the  $x$ - and the  $z$ -directions which are both of the order of  $\delta$ ; they are inclined to the wall at an angle that varies between  $20^\circ$  and  $45^\circ$ , depending on the unsteadiness of the motion and the distance from the wall, and they are separated from each other in the streamwise direction by deep indentations, into which irrotational fluid from outside the boundary layer is entrained. The fluid in the bulges undergoes a slow ‘overturning’ motion, driven by the shear, so that the fluid on the downstream side of the bulge (the leading edge of the structure) moves towards the wall and the fluid on the trailing edge moves away from the wall; the back of the structure is a zone of relatively intense shear. The bulges are transported by the mean flow with an average velocity  $U_C$  of about  $0.8 U_\infty$  in the outer layer, and  $0.6-0.7 U_\infty$  in the logarithmic layer.

The two most important features that emerge from these visualizations are that bubble migration starts as the bubble penetrates the trailing edge of a bulge, and that as it

migrates towards the wall it moves through the bulge, so that it actually impacts on the wall near the leading edge of the bulge that it has just traversed, in the indentation that separates the bulge from the one immediately preceding it. This is illustrated schematically in Fig. 15.

In order to provide quantitative confirmation of the observed behaviour, we have analysed the filmed trajectories in three ways, so as to compute:

- the correlation between the positions of the migrating bubbles and the turbulent bulges;
- the correlation between the point of bubble impact on the plate and the position of the indentations between the bulges;
- the length and time scales of the migration trajectories relative to the characteristic length and time scales for the turbulent structures.

To compute the correlation between bubble migration and the passage of the turbulent bulges we have defined, for each sequence, a structure-migration coefficient, which is defined as the number of migrations occurring within the bulges, divided by the total number of migrations observed during the sequence. If the relationship between these two processes was purely deterministic, and if our measurements were sufficiently accurate, we ought to obtain the same value of the structure-migration coefficient for each sequence, but of course neither of these conditions is true, and so we expect some variability in the coefficient, from one sequence to the next. The histogram of this coefficient has been plotted in Fig. 16, which shows that the coefficient varies from about 0.5 to 0.8, with about 80% of the sequences providing a value greater than 0.6. There are three main reasons for the scatter in the results. The first is that both the turbulent structures and the bubble trajectories are variable, so that even if there is a mechanistic influence of one on the other, it does not follow that bubble migrations will only occur within the structures. The second

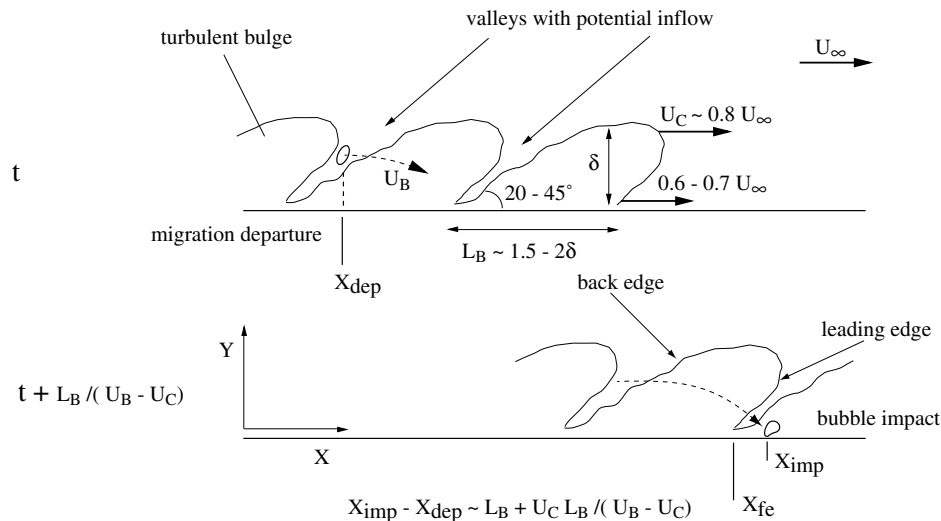


Fig. 15. Average characteristics of the large scale turbulent structures and most frequently observed scenario for the bubble migration.

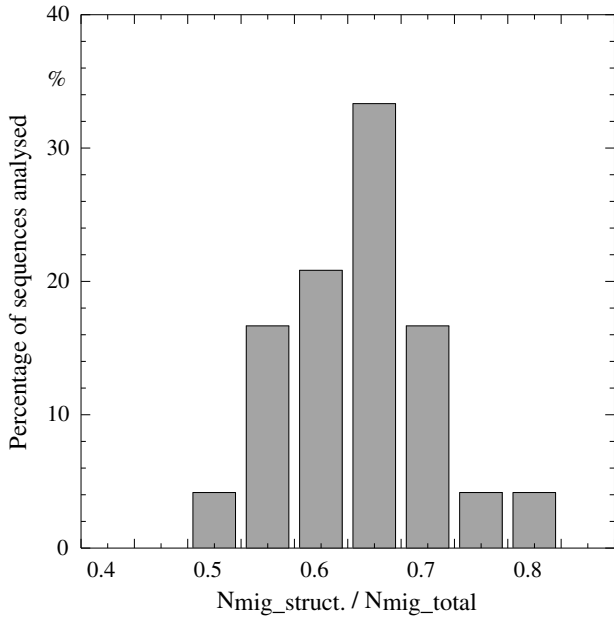


Fig. 16. Number of migrations across the structures divided by the total number of migrations visually identified per sequence. Analysis of 24 sequences of 5.452 s (455 migrations).  $U_\infty = 1 \text{ m s}^{-1}$ .

reason is that the visualization technique does not provide a perfect indication of the outer boundaries of the intermittent structures; the dye diffuses, and the structures deform, so that, in general, we underestimate the extent of the structures. This leads to an underestimate of the correlation, since some of the trajectories that we class as outside the structure will, in fact, be inside an imperfectly defined structure. The third reason is that the bubble trajectories and the structures are both 3D, and we are basing our analysis only on bubbles that remain in the visualization plane throughout the migration. Thus we have rejected trajectories that leave the light plane, even though the bubble might remain within the structure for the remainder of its migration. This will also lead to an underestimate of the correlation coefficient.

The correlation between the point at which the migrating bubble reached the wall and the position of the indentation between two bulges was computed for both free stream velocities, in each case from an ensemble of 250 trajectories, selected so that the bubble, its shadow and the structure were all clearly visible in the moment preceding the impact. For each impact we have measured the distance between the point of impact  $X_{\text{imp}}$  and the position of the indentation,  $X_{\text{fei}}$ , defined as the position of the leading edge of the bulge traversed by the bubble during its migration. In order to compare the results for the two free stream velocities this distance has been scaled by the average length of the bulges,  $L_B$ , as measured from the different films; the histogram of this length, scaled on  $\delta$ , is shown in Fig. 17, from which we conclude that  $L_B/\delta \sim 1.5$ , which is in agreement with previous studies of single phase flow at similar Reynolds numbers (Kovasnay et al., 1970). The histogram of the scaled impact distances  $(X_{\text{imp}} - X_{\text{fei}})/L_B$  is

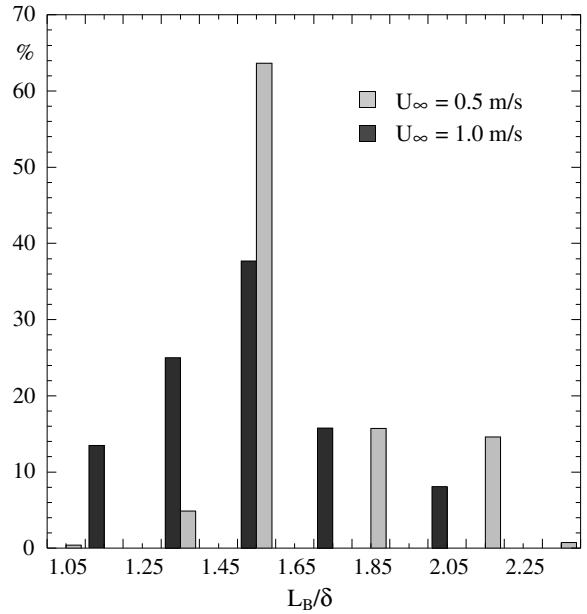


Fig. 17. Histogram of the length of the bulges. The most probable length is  $L_B = 1.5\delta$ .

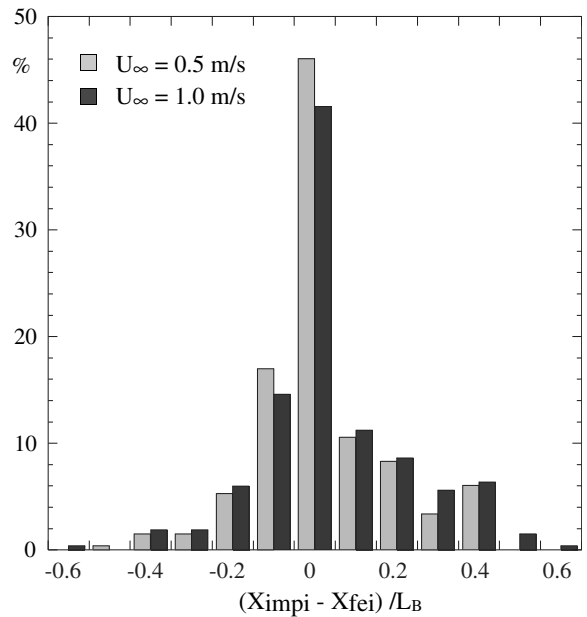


Fig. 18. Histogram of the normalised distance between the point of bubble impact  $X_{\text{imp}}$  and the leading edge of the bulge traversed by the bubble during its migration,  $X_{\text{fei}}$ . The average length of the bulges is  $L_B = 1.5\delta$ . Statistics from 250 trajectories.

shown in Fig. 18; there is a sharp peak around zero, indicating a strong correlation between the impact point and the indentation between the bulges. This correlation was also indirectly demonstrated in Tran-Cong (1999) and Tran-Cong et al. (2001), by comparing positions of the impacts with the positions of the indentations, as predicted with a simple kinematics model of their motion.

The strong correlation between the point at which bubbles reach the wall and the indentations between the bulges

suggests that once a bubble enters a bulge, it is ‘captured’ by the bulge, and its subsequent trajectory is strongly determined by the internal dynamics of the flow within the bulge. An interesting question, therefore, is whether the bulges are involved in entraining bubbles from outside the boundary layer, or whether they simply capture and ‘manipulate’ the bubbles that traverse them. Tran-Cong (1999) showed that the time scale for bubble migration was of the same order as the timescale of the bursting cycle in the boundary layer (Blackwelder and Haritonidis, 1983), which suggests some sort of deterministic relationship between the two processes. To test this further, we have computed the time taken for the migrating bubbles to travel the length of the bulge, and from this, the point at which the bubbles enter the bulge. If the bulges entrain bubbles, then we would expect them to enter the bulges at roughly the same point, as indicated schematically in Fig. 15. If, on the other hand, the bulges simply modify the trajectories of migrating bubbles, then we would expect there to be much greater variation in the point at which the bubbles enter the bulge, and in the time spent by the bubble in the bulge. The relative motion of the bubble across the bulge is most easily calculated in a frame of reference moving with the average convection speed of the bulge,  $U_C$ ; the bubble velocity then becomes  $(U_B(t) - U_C)$  and the time  $T_C$  for the bubble to travel the length of the bulge  $L_B$  is given by the solution to the equation:

$$\int_{-T_C}^0 [U_B(t) - U_C] dt = L_B. \quad (2)$$

Here we have taken  $L_B = 1.5\delta$  and  $U_C = 0.7U_\infty$ ; the bulges deform as they move, because of the velocity gradient across the boundary layer, and there is no single value of the convection velocity that is representative of the motion of the entire bulge, so the value of  $U_C = 0.7U_\infty$  was chosen as a compromise between the velocities in the inner and the outer layers. For each of the experimental conditions, we have integrated the measured average bubble velocities  $U_B(t)$  backwards in time, until Eq. (2) is satisfied. This then provides us with a length scale,  $L_B + U_C T_C$ , and a time scale,  $T_C$ , for each of the average trajectories. The bubble trajectories and displacements for the different experimental conditions have been plotted in Figs. 19 and 20, scaled on these variables and the boundary layer thickness  $\delta$ . If these figures are compared with the corresponding dimensional representations (Figs. 11 and 12) then it is clear that with this scaling the trajectories for the different conditions all collapse onto a single, universal form, and there is no Reynolds number dependence. This is particularly evident for the region  $Y/\delta \sim 0.3-0.4$ . The dimensionless time and length scales that characterize these migration trajectories are both close to unity ( $\sim 1.2$ ), for all bubble diameters and values of  $U_\infty$ , confirming that the scaling is consistent with the physical processes involved. A structure velocity  $U_C = 0.8 U_\infty$  would yield values still closer to unity, but this would be less representative of the motion of the bulges near the wall. The

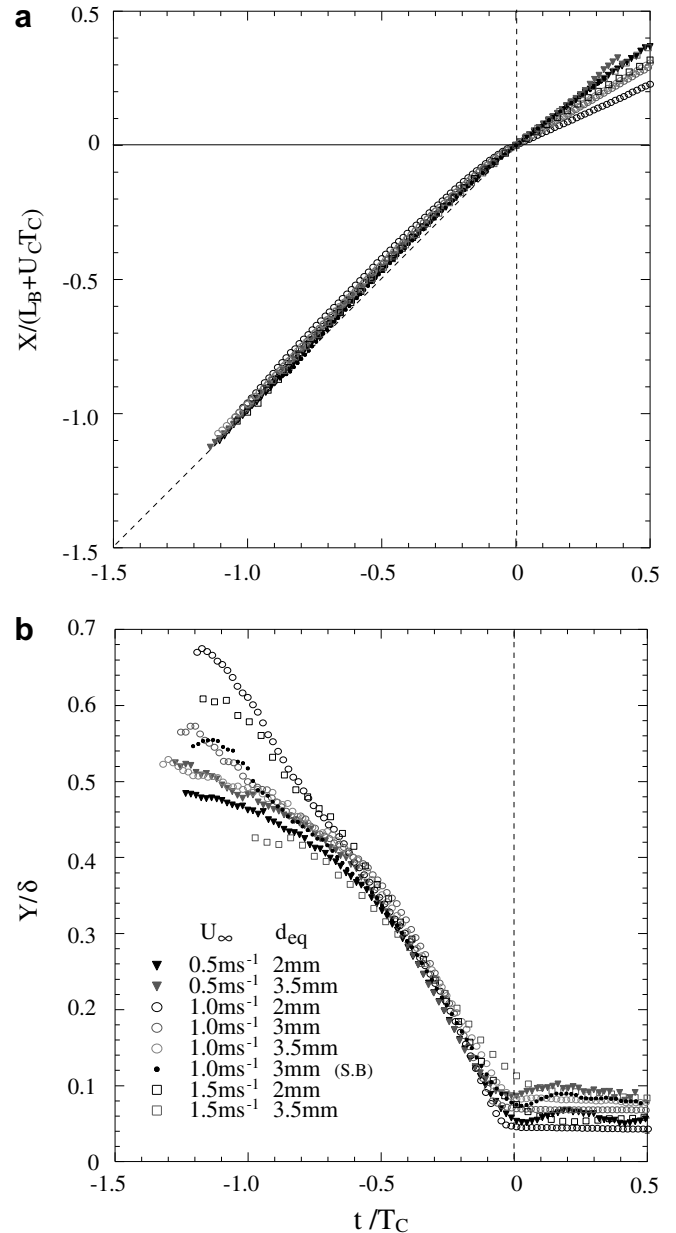


Fig. 19. Non-dimensional coordinates of the mean Lagrangian trajectories of migration. Tcross: mean crossing time of the large turbulent structures (size  $L_X = 1.5\delta$ , velocity  $U_C = 0.7 U_\infty$ ) by the bubbles.

streamwise displacement of the bubble  $X(t^*)/[L_B + U_C T_C]$  varies almost linearly with the dimensionless time  $t^* = t/T_C$  before the impact with the wall (Fig. 19a), so the variation in  $Y/\delta$  as a function of  $t^*$  (Fig. 19) is almost equivalent for  $t^* < 0$ , to the bubble trajectory  $Y/\delta$  as a function of  $[X(t) - U_C t]/L_B$ , in a frame of reference moving with the convection velocity of the bulges.

The results of this analysis of the measured bubble trajectories are all consistent with the hypothesis that the unsteady structures of the boundary layer are involved in the migration of bubbles towards the wall, but they do not explain the underlying mechanisms involved in the process. The flow visualizations that we have performed give a global

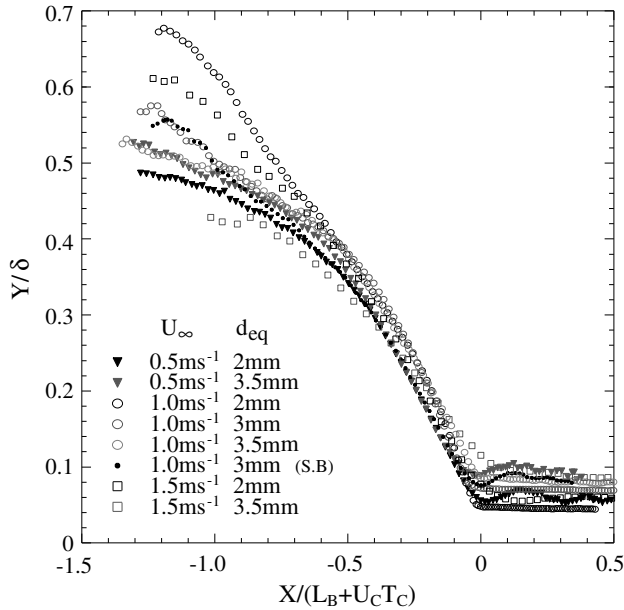


Fig. 20. Non-dimensional Lagrangian trajectories of migration. Tcross: mean crossing time of the large turbulent structures (size  $L_x = 1.5\delta$ , velocity  $U_C = 0.7U_\infty$ ) by the bubbles.

view of the outer edge of the large unsteady structures, but no information on the complex fluid motion developing inside, and its interaction with the near wall turbulence. Additional measurements of the instantaneous velocity flow field around the bubbles would be useful to complete the study and determine the forces involved in the migration. There have already been some attempts to do this; Felton and Loth (2002), for example, used a standard PIV system to investigate the motion of 1 mm diameter bubbles in a boundary layer. But the timescale for bubble migration in our experiments is much shorter ( $\sim 0.12$  s) and trajectories typically 3D, so similar measurements would require a time-resolved stereoscopic PIV system. Without such measurements, the entrainment of the bubbles in the bulges remains difficult to explain.

The bubbles begin to migrate whilst they are still relatively far from the wall – typically between  $0.5\delta$  and  $0.7\delta$  from the wall, and in a significant number of realisations they began to migrate at  $\delta$ , so the coherent structures such quasi-streamwise or hairpin vortices which are typically found at 100–200 wall units from the wall layer cannot be involved in the first stages of migration. The formation of these structures is characterised by cycles of ejections and sweeps (Robinson, 1991; Adrian et al., 2000), and the shear layers associated with this give rise to patterns of alternating low and high pressure but these also remain localized near to the wall, and thus can hardly influence the initial stages of migration. The initiating processes must therefore be located in the outer layer. The slow overturning large scale motion existing beneath the interface of the bulges, which contributes to the entrainment of non-turbulent flow in the valleys (Head and Bandhyopadhyay, 1981),

could possibly drive the bubbles towards the wall. This mechanism would be consistent with the location of the impacts of the bubbles seen on the films. However, the vorticity of this mean rotational motion is, *a priori*, too weak to induce local lift effects which could explain the sudden departures of the 2 mm diameter bubbles (Figs. 7a and 13b). Besides, the inflow induced near the front edge is relatively weak, typically of the order of  $0.03U_\infty$  (Kovasnay et al., 1970) in the outer layer, and hardly sufficient to drag the bubbles with wall-normal velocities such those we have measured (Fig. 13b, Table 3). Another possible explanation could be provided by an interaction between the bubbles and the velocity fields associated with coherent span-wise vortices, such as the heads of hairpin vortices, populating the outer region. Recent high spatial resolution PIV measurements by Adrian et al. (2000) at  $Re_\theta = 930, 2370, 6845$  (similar to our experiment), have shown that the bulges are formed by packets of hairpin vortices, initially created at the wall during the bursting cycle process, confirming the results from previous studies by Robinson (1991) and Head and Bandhyopadhyay (1981). These packets can grow up to  $0.8\delta$ , where they define the instantaneous outer edge of the boundary layer, and can be as long as  $2\delta$  in the  $x$ -direction. These packets are travelling at velocities that range from  $0.5$ – $0.6 U_\infty$  to  $0.8 U_\infty$  according to their distance from the wall, and the number of hairpin vortices in a packet increases with increasing Reynolds number. Within each packet, the flows induced by the vorticity in the cores of the hairpin vortices combine coherently to generate a region of reverse flow close to the wall, with relatively uniform momentum. One possible explanation for the migration of these bubbles, therefore, is that as the bubbles rise their natural oscillations carry them into the regions of locally concentrated vorticity in the packets near the backs of the bulges which cause an initial deviation and begin the migration. The bubbles are then driven to the surface under the increasing influence of the mean shear induced lift force. But for the moment this remains a conjecture, and more detailed measurements of the interaction between a bubble and the surrounding velocity field are needed to confirm this.

#### 4. Conclusions

Bubble migration across an up-flowing turbulent boundary layer on a flat plate has been studied by measuring the trajectories of migrating bubbles, together with simultaneous visualization of the instantaneous structures of the boundary layer. The bubbles were mono-disperse released singly, or in low void fraction flows. Investigations were performed in both laminar and turbulent regimes, with bubbles in a diameter range corresponding to two families of shape and motion in quiescent tap water – ellipsoidal bubbles ( $2 \text{ mm} \leq d_{eq} \leq 4 \text{ mm}$ ;  $1.7 \leq We \leq 3.4$ ), for which the trajectories are essentially helicoidal, and larger, highly deformable bubbles ( $d_{eq} \geq 4 \text{ mm}$ ;  $We \geq 3.4$ ) for

which the trajectories are almost rectilinear with a rocking motion.

The results show clearly that bubble migration, defined as a sudden deflection towards the wall followed by trapping of the bubble at the surface, only takes place for small bubbles with diameters less than 3.5 mm and has a non-systematic character. The deflections towards the wall follow non-deterministic trajectories in the sense that they differ significantly from one bubble to another, and occur on a short time scale. A significant number of them start near the edge of the boundary layer, where the mean shear is weak, excluding the possibility that a mean shear-induced lift force could be the driving force to the wall in this part of the flow. On the other hand, deflection and trapping become systematic when the bubbles are released in the high shear region (buffer and logarithmic region). All these observations suggest that migration might result from the combination of two mechanisms; one, involving turbulence, which drives bubbles close to the inner layer in a non-deterministic way and the other, involving the mean shear, which traps them inside. The mean shear-induced lift force could play a role in this second mechanism and would explain the absence of trapping reported in downward pipe flows. Some bubbles larger than 4 mm still migrate to the wall but the trajectories do not correspond to the definition of a true migration and these bubbles are never trapped at the surface. The critical diameter  $3.5 \text{ mm} < d_{\text{eqcrit}} < 4 \text{ mm}$  for the change in behaviour corresponds to the size for which bubbles become highly deformable and cannot be trapped at the wall, sliding along it, even when released at the surface. This critical diameter is very close to the thickness of the region of high shear close to the wall.

The migrations observed with isolated bubbles exhibit the same characteristics, proving that bubble–bubble interactions do not play a significant role for the conditions investigated here. The study of the influence of the flow regime demonstrates that in our experiments migration never occurs in laminar flow and increases with Reynolds number, as the flow becomes more turbulent. The critical diameter for the bubble trapping does not change with increasing Reynolds number, one possible reason being that the thickness of the region of high shear also remains sensibly constant. Visualizations of the structures show clearly that, on average, the small bubbles are entrained towards the wall as they cross the large scale unsteady 3D structures of the boundary layer ('bulges'). Other results provide quantitative support for this analysis. The impact location on the plate correlates well with the locations of the deep valleys separating the structures and the average time of migration calculated from the mean Lagrangian trajectories coincides with the mean transit time of the bubbles across the structures, for all Reynolds numbers investigated here. If the trajectories are scaled on this transit time and the boundary layer thickness  $\delta$  they become independent of Reynolds number for a region of the flow extending up to  $Y \sim 0.3\text{--}0.4\delta$ .

The reasons for the entrainment of bubbles into the bulges are still unclear, because the visualizations do not

provide any information on the complex turbulent fluid motion which occurs within the bulges. It would therefore be useful to measure the instantaneous velocity flow field around the bubbles, since this would enable us to estimate the instantaneous forces involved in the migration; time resolved stereoscopic PIV techniques could be very useful for this problem.

### Acknowledgements

This work was funded by the Centre National de la Recherche Scientifique (Gredic). The authors wish to thank Pr. M. Lance and Pr J. Bataille for their helpful comments and suggestions and D. Echampard, M. Gaud., P. Dutheil for their technical assistance.

### References

- Adrian, R.J., Meinhart, C.D., Tomkins, C.D., 2000. Vortex organisation in the outer region of the turbulent boundary layer. *J. Fluid Mech.* 422, 1–54.
- Auton, T.R., Hunt, J.C.R., Prud'homme, M., 1988. The force exerted on a body in inviscid unsteady non-uniform rotational flow. *J. Fluid Mech.* 197, 241–257.
- Blackwelder, R.F., Haritonidis, J.H., 1983. Scaling the bursting frequency in turbulent boundary layers. *J. Fluid Mech.* 132, 87–103.
- Clift, R., Grace, J.R., Weber, M.E., 1978. *Bubbles, Drops, and Particles*. Academic Press, New York.
- Colin, C., Kamp, A., Fabre, J., 1993. Influence of gravity on void and velocity distribution in two-phase gas–liquid flow in pipe. *Adv. Space Res.* 13, 141–145.
- Ellingsen, K., Risso, F., 2001. On the rise of an ellipsoidal bubble in water: oscillatory paths and liquid-induced velocity. *J. Fluid Mech.* 440, 235–268.
- Ervin, E.A., Tryggvason, G., 1997. The rise of bubbles in a vertical shear flow. *ASME J. Fluid Eng.* 119, 443–449.
- Felton, K., Loth, E., 2001. Spherical bubble motion in a turbulent boundary layer. *Phys. Fluids* 13, 2564–2577.
- Felton, K., Loth, E., 2002. Diffusion of spherical bubbles in a turbulent boundary layer. *Int. J. Multiphase Flow* 28, 69–92.
- Ganchev, B.G., Peresadko, V.G., 1985. Hydrodynamic and heat transfer processes in descending bubble flows. *J. Eng. Phys.* 49, 181–189.
- Grossetete, C., 1995. *Caractérisation expérimentale et simulation de l'évolution d'un écoulement diphasique à bulles ascendant dans une conduite verticale*. Thèse Ecole Centrale de Lyon.
- Head, M.R., Bandhyopadhyay, P., 1981. New aspects of turbulent boundary-layer structure. *J. Fluid Mech.* 107, 297–338.
- Herringe, R.A., Davis, M.R., 1976. Structural development of gas–liquid mixture flows. *J. Fluid Mech.* 73, 97–123.
- Kariyasaki, A., 1987. Behaviour of a single gas bubble in a liquid flow with linear velocity profile. In: *Proceedings of the 1987 ASME-JSME Thermal Engineering Joint Conference*, ASME, New-York, NY, vol. 5, pp. 261–267.
- Kashinsky, O.N., Timkin, L.S., Cartellier, A., 1993. Experimental study of laminar bubbly flow in vertical pipe. *Exp. Fluids* 15, 308–314.
- Kashinsky, O.N., Randin, V.V., 1999. Downward bubbly gas–liquid flow in vertical pipe. *Int. J. Multiphase Flow* 25, 109–138.
- Kovasnay, L.S.G., Kibens, V., Blackwelder, R.F., 1970. Large scale motion in the intermittent region of a turbulent boundary layer. *J. Fluid Mech.* 41, 283–325.
- Lance, M., Bataille, J., 1991. Turbulence in the liquid phase of a uniform bubbly air–water flow. *J. Fluid Mech.* 222, 95–118.
- Liu, T.J., 1993. Bubble size and entrance length effects on void development in a vertical channel. *Int. J. Multiphase Flow* 19, 99–113.

- Liu, T.J., 1997. Investigation of the wall shear stress in vertical bubbly flow under different bubble size condition. *Int. J. Multiphase Flow* 23, 1085–1109.
- Lunde, K., Perkins, R.J., 1995. A method for the detailed study of bubble motion and deformation. In: Serizawa, A., Fukano, T., Bataille, J. (Eds.), *Advances in Multiphase Flow*. Elsevier, pp. 395–405.
- Marié, J.L., Moursali, E., Tran-Cong, S., 1997. Similarity law and turbulence intensity profiles in a bubbly boundary layer at low void fraction. *Int. J. Multiphase Flow* 23, 227–247.
- Milne-Thomson, L.M., 1968. *Theoretical Hydrodynamics*. Macmillan.
- Moursali, E., Marié, J.L., Bataille, J., 1995. An upward turbulent bubbly boundary layer along a vertical flat plate. *Int. J. Multiphase Flow* 21, 107–117.
- Nakoryakov, V.E., Kashinsky, O.N., Burdukov, A.P., Odnoral, V.P., 1981. Local characteristics of upward gas–liquid flows. *Int. J. Multiphase Flow* 7, 63–81.
- Nikitopoulos, D.E., Fiedler, J., Dowden, M., Evans, E., 2004. Bubble motion characteristics in Vertical-upwards pipe flow. In: *Proceeding of the 5th International Conference on Multiphase Flow, ICMF'04*, Yokohama.
- Perkins, R.J., Hunt, J.C.R., 1989. Particle tracking in turbulent flows. In: Fernholz, H.H., Fiedler, H.E. (Eds.), *Advances in Turbulence*, vol. 2. Springer-Verlag, pp. 286–291.
- Robinson, S.K., 1991. Coherent motion in the turbulent boundary layer. *Ann. Rev. Fluid Mech.* 23, 601–639.
- Saffman, P.G., 1965. The lift on a small sphere in a slow shear flow. *J. Fluid Mech.* 22, 385–400.
- Sato, Y., Honda, T., Yoshinaga, T., Saruwatari, S., 1976. An experimental investigation of air bubble motion in water streams in vertical ducts: part I & II. *Tech. Rep. Kumamoto University* 25, 2, 97–114. (in Japanese).
- Schlichting, H., 1968. *Boundary Layer Theory*, sixth ed. McGraw-Hill, New York.
- Schiller, L., Nauman, A., 1933. Über die grundlegenden Berechnungen bei der Schwerkraftaufbereitung. *Zeitschrift der VDI*, 77.
- Sekoguchi, K., Sato, Y., Honda, T., 1974. An experimental investigation on bubble flow. *Trans. Japan Soc. Mech. Eng.* 40, 1395–1403 (in Japanese).
- Sekoguchi, K., Fukui, H., Sato, Y., 1979. Flow characteristics and heat transfer in vertical bubble flow. In: *Proceedings of the Japan-US seminar on Two-Phase Flow Dynamics*, Kansai, Japan, pp. 59–74.
- Serizawa, A., Kataoka, I., Michiyoshi, I., 1975. Turbulence structure of air–water bubbly flow. Part I, II & III. *Int. J. Multiphase Flow* 2, 221–259.
- Serizawa, A., Kataoka, I., 1988. Phase distribution in two-phase flow. In: Afgan, N.H. (Ed.), *Transient Phenomena in Multiphase Flow*. Hemisphere Pub. Corp., NY, pp. 179–225.
- Tennekes, H., Lumley, J.L., 1972. *A First Course in Turbulence*. MIT Press, Cambridge, Mass, pp. 146–196.
- Tomiyama, A., Sou, A., Zun, I., Kanami, N., Sakagushi, I., 1995. Effects of Eötvös number and dimensionless volumetric flux on lateral motion of a bubble in a laminar flow. In: *Proceedings of the 2nd International Conference on Multiphase Flow, ICMF'02*, 2, Kyoto, pp. PD11–PD18.
- Tran-Cong, S., Marié, J.L., Perkins, R.J., 1998. Experimental study of the bubble motion in an upward turbulent boundary layer. In: *Proceedings of the 3rd International Conference on Multiphase Flow, ICMF'98*, Lyon, pdf 682.
- Tran-Cong, S., 1999. *Comportement de bulles d'air dans un écoulement ascendant turbulent, au voisinage d'une plaque plane*. Thèse de doctorat de l'Université Claude–Bernard, Lyon I.
- Tran-Cong, S., Marié, J.L., Perkins, R.J., 2001. Bubble migration in a turbulent boundary layer. In: *Proceedings of the 4th International Conference on Multiphase Flow, ICMF'01*, New-Orleans, pdf 197.
- Wang, S.K., Lee, S.J., Jones, O.C., Lahey, R.T., 1987. 3D turbulence structure and phase distribution measurements in bubbly two-phase flows. *Int. J. Multiphase Flow* 13, 327–343.
- Zaruba, A., Lucas, D., Prasser, H.-M., Höhne, T., 2007. Bubble–wall interactions in a vertical gas–liquid flow: bouncing, sliding and bubble deformations. *Chemical Engineering Science* 62, 1591–1605.
- Zun, I., 1980. The transverse migration of bubbles influenced by walls in vertical bubbly flow. *Int. J. Multiphase Flow* 6, 583–588.
- Zun, I., 1988. Transition from wall void peaking to core void peaking in turbulent bubbly flow. In: Afgan, N.H. (Ed.), *Transient Phenomena in Multiphase Flow, ICHMT Int Seminar*. Hemisphere Pub. Corp., Washington, DC, pp. 225–245.
- Zun, I., 1990. The mechanism of bubble non-homogeneous distribution in two-phase shear flow. *Nuclear Eng. Design* 118, 155–162.